

A SiO $J = 5 \rightarrow 4$ SURVEY TOWARD MASSIVE STAR FORMATION REGIONS

SHANGHUO LI^{1,2,3}, JUNZHI WANG^{1,4}, MIN FANG⁵, QIZHOU ZHANG², FEI LI^{1,3}, ZHI-YU ZHANG^{6,7}, JUAN LI¹, QINGFENG ZHU⁸, AND SHAOSHAN ZENG⁹

¹Shanghai Astronomical Observatory, Chinese Academy of Sciences, 80 Nandan Road, Shanghai 200030, China

²Center for Astrophysics | Harvard & Smithsonian, 60 Garden Street, Cambridge, MA 02138, USA

³University of Chinese Academy of Sciences, 19A Yuquanlu, Beijing 100049, China

⁴Key Laboratory of Radio Astronomy, Chinese Academy of Sciences, 210008, Nanjing, China

⁵Department of Astronomy and Steward Observatory, University of Arizona, 933 N Cherry Ave., Tucson, AZ 85721, USA

⁶Institute for Astronomy, University of Edinburgh, Blackford Hill, Edinburgh, EH9 3HJ, UK

⁷European Southern Observatory, Karl-Schwarzschild-Strasse 2, D-85748 Garching, Germany

⁸Astronomy Department, University of Science and Technology, Chinese Academy of Sciences, Hefei 210008, China

⁹School of Physics and Astronomy, Queen Mary University of London, Mile End Road, E1 4NS London, UK

ABSTRACT

We performed a survey in the SiO $J = 5 \rightarrow 4$ line toward a sample of 199 Galactic massive star-forming regions at different evolutionary stages with the SMT 10 m and CSO 10.4 m telescopes. The sample consists of 44 infrared dark clouds (IRDCs), 86 protostellar candidates, and 69 young HII regions. We detected SiO $J = 5 \rightarrow 4$ line emission in 102 sources, with a detection rate of 57%, 37%, and 65% for IRDCs, protostellar candidates, and young HII regions, respectively. We find both broad line with Full Widths at Zero Power (FWZP) $> 20 \text{ km s}^{-1}$ and narrow line emissions of SiO in objects at various evolutionary stages, likely associated with high-velocity shocks and low-velocity shocks, respectively. The SiO luminosities do not show apparent differences among various evolutionary stages in our sample. We find no correlation between the SiO abundance and the luminosity-to-mass ratio, indicating that the SiO abundance does not vary significantly in regions at different evolutionary stages of star formation.

Keywords: ISM: clouds – ISM: jets and outflows – ISM: molecules – submillimeter: ISM – stars: formation – stars: massive

1. INTRODUCTION

The formation of massive stars has been studied both observationally and theoretically for several decades (Habing & Israel, 1979; Mac Low & Klessen, 2004; McKee & Ostriker, 2007; Bergin & Tafalla, 2007; Motte et al., 2018). However, from an observational point of view, it is challenging to study the formation mechanism due to the large distance, the high extinction, and the short timescales of massive star formation (Zinnecker & Yorke, 2007; Motte et al., 2018). This has limited our understanding of the processes that regulate massive star formation. Massive star formation can produce strong feedback to their parent molecular clouds and surrounding interstellar medium (ISM) in form of jets, outflows, ultra-violet radiation, and HII regions. (Churchwell, 2002; Arce et al., 2007; Zhang et al., 2015; Bally, 2016; Li et al., 2017). These feedbacks also provide crucial clues to the massive star formation processes.

Interactions between jets/outflows and surrounding

medium have been found in massive star forming regions at multiple evolutionary stages – from infrared dark clouds (IRDCs) to HII regions (Churchwell, 2002; Arce et al., 2007; Qiu et al., 2007; Pillai et al., 2011; Zhang et al., 2015; Bally, 2016; Louvet et al., 2016; Li et al., 2017). A number of gas tracers has been employed to study shocks in the interactions. Superior to the CO and HCO⁺ lines which are often contaminated by the emission from the ambient material, the rotational transitions of Silicon monoxide (SiO) have been widely used in studying shock conditions, especially those associated with protostellar jets and outflows (Cesaroni et al., 1999; Zhang et al., 1999; Lesaffre et al., 2013; Leurini et al., 2014; Codella et al., 2013; Maud et al., 2018). This is because that shock activities release Si atoms from dust grains into gas phase via sputtering or vaporisation (Gusdorf et al., 2008a,b). Then SiO molecules are formed dominantly by the reaction between Si and O₂ and OH in the gas phase (Herbst et al., 1989; Caselli et al., 1997; Schilke et al., 1997; Le Picard et al., 2001; Rivero-Santamaría et al., 2014). Alternatively, SiO can also be formed via less prominent routes that involve Si⁺ (OH, H), SiO⁺ (H₂, H) and HSiO⁺ (e, H) (Leurini et al., 2013).

The SiO abundance in molecular outflows can be enhanced by up to six orders of magnitude relative to that in the quiescent regions (Martin-Pintado et al., 1992; Gibb & Hoare, 2007; López-Sepulcre et al., 2011). This makes SiO an excellent tracer for investigating shock activities in star formation regions. SiO has been used to trace shocks with different velocities (low-velocity: $v \leq 10 \text{ km s}^{-1}$, medium-velocity: $v \sim 10 - 20 \text{ km s}^{-1}$, high-velocity: $v \sim 20 - 50 \text{ km s}^{-1}$, and extremely high-velocity: $v \sim 100 \text{ km s}^{-1}$). The low- and medium-velocity shocks could be associated with outflows (Li et al., 2017), converging flows (Jiménez-Serra et al., 2010; Henshaw et al., 2013) and cloud collision (Louvet et al., 2016). The high-velocity shocks, on the other hand, are most likely associated with jets and molecular outflows driven by embedded young stars (Qiu et al., 2007). The extremely high-velocity shocks have been found in the Central Molecular Zone (CMZ) of our Galaxy, which is likely associated with larger-scale shocks in the CMZ (Martín-Pintado et al., 1997; Jones et al., 2012).

Observations of the SiO emission toward various evolutionary stages of star formation would allow us to characterize the variation in SiO with evolution. Observations of the SiO $J = 2 \rightarrow 1$ line toward a sample of massive star formation regions by Sakai et al. (2010) found that mid-infrared bright sources tend to have a lower SiO abundance than that of mid-infrared dark sources, indicating that the SiO abundance decreases in more evolved massive star formation regions. A similar decreasing trend in the SiO abundance with time has been reported by several studies of samples at different evolutionary stages (Miettinen et al., 2006; Motte et al., 2007; Sánchez-Monge et al., 2013; López-Sepulcre et al., 2011). On the other hand, other studies found a different trend that the SiO abundance in infrared-bright clumps is higher than the one in infrared-quiet clumps (e.g., Gerner et al., 2014; Miettinen, 2014), or the SiO abundance does not vary significantly among different evolutionary stages of massive star formation (Sanhueza et al., 2012; Leurini et al., 2014; Csengeri et al., 2016). Therefore, it is still under debate if the SiO abundance varies with the evolutionary stages of massive star formation.

The SiO 5-4 transition is an excellent tracer to study strong shock activities that are related to outflows/jets driven by embedded massive protostars, since it requires higher excitation conditions (a critical density $n_{cr} \sim 1.7 \times 10^6 \text{ cm}^{-3}$, upper energy level $E_u = 31.26 \text{ K}$) than those of CO, HCO⁺ and SiO low J transitions. In this work, we report a survey in the SiO 5-4 line of 199 massive clumps at different stages of massive star formations, e.g., IRDCs, protostellar candidates, and HII regions, with the SMT 10 meter and CSO 10.4 meter telescopes. First we describe the sample selection and observations in § 2. Then, we present the data analysis and results in § 3. We discuss the observational results in § 4, and summarize the main findings in § 5.

2. SAMPLES AND OBSERVATIONS

2.1. The sample

Our targets are selected from several catalogs in the literature that can be grouped into three evolutionary stages of massive star formation: IRDCs, protostellar phase and HII regions. The detailed information of the sample is described as follows:

IRDCs: We selected 44 massive clumps from Sakai et al. (2008), which are identified as silhouettes against the bright Galactic background in the $8 \mu\text{m}$ band of the Midcourse Space Experiment (MSX). These objects are within a distance of 4.3 kpc (Beuther et al., 2005). Among this IRDC sample, 32 sources were observed in the Spitzer $24 \mu\text{m}$ band, and 25 of them show point-like sources in the $24 \mu\text{m}$ images (Sakai et al., 2008), indicating star formation in these regions. Since massive IRDCs are cold ($< 20 \text{ K}$) and dense ($> 10^5 \text{ cm}^{-3}$) (Pillai et al., 2006; Bergin & Tafalla, 2007), they are considered the precursors of massive stars and star clusters.

Protostars: A subset (86) of our sample are massive clumps associated with protostellar candidates (protostars), which are originally selected from the IRAS point source catalog. Among them, 38 sources are retrieved from Zhang et al. (2005), 19 sources from Sridharan et al. (2002), and 29 sources from Maud et al. (2015b) and Lumsden et al. (2013). The distances of these sources lie in the range of 0.7 to 8.7 kpc (Zhang et al., 2005; Sridharan et al., 2002; Maud et al., 2015b; Lumsden et al., 2013; Reid et al., 2014). Eighty-one sources out of 86 protostars exhibit CO outflow signatures (Zhang et al., 2005; Sridharan et al., 2002; Maud et al., 2015b; Lumsden et al., 2013). Without associated HII regions (Maršáľková, 1974; Altenhoff et al., 1979; Griffith et al., 1994; Wright et al., 1994), this subsample is believed to be at the intermediate evolutionary stage between IRDCs and HII regions (Sridharan et al., 2002; Zhang et al., 2005; Maud et al., 2015a).

HII regions: Sixty-nine massive clumps are selected from the UC HII, CHII and HII region catalogs (Shirley et al., 2003; Li et al., 2015; Maud et al., 2015b; Lumsden et al., 2013). The distances of these sources lie in the range of 1.2 to 7.6 kpc. Most of them (43) are associated with H₂O maser emission (Cesaroni et al., 1988; Shirley et al., 2003). The sources in this subsample are considered in the most advanced evolutionary stage in our sample.

2.2. Observations

2.2.1. CSO 10.5 m observations

Sixteen sources were observed in the SiO 5-4 transition at a rest frequency of 217.104984 GHz using the Caltech Submillimeter Observatory's (CSO)¹ 10.4 m telescope in 2013 (see

¹ <http://cso.caltech.edu/>

Table 1). In order to achieve good spectral baselines, we used the standard position switching mode with the ‘clean’ reference position (OFF source) 30 arcmin offset from the source in azimuth. The typical on-source time is about 10 minutes for each target. The Fast Fourier Transform Spectrometer provides a 4 GHz window of double-side band (DSB) coverage with a velocity resolution of 0.27 MHz (0.37 km s^{-1} at 217 GHz). The SiO 5-4 transition was covered in the lower-side band (LSB). Typical system temperatures range from 250 to 400 K, and the typical rms noise ($\delta_{T_{\text{mb}}}$) is between 0.03 and 0.14 K at a velocity resolution of 0.37 km s^{-1} . The full-width half-maximum (FWHM) beam size is about $27.4''$ at the observing frequency of 217.1 GHz. Data reduction was performed with the CLASS package, which is a part of the GILDAS² software. The data were converted from the antenna temperature, T_A^* , to the main-beam temperature, T_{mb} , using $T_{\text{mb}} = T_A^*/\eta_{\text{mb}}$, where $\eta_{\text{mb}} = 0.69$ is the beam efficiency measured by the CSO. More detailed information of observations and data reduction is described in Li et al. (2015).

2.2.2. SMT 10 m observations

Additional observations toward 185 objects were obtained in the SiO 5-4 transition using the Heinrich Hertz Submillimeter Telescope (SMT)³ 10 m telescope in 2015 and 2016 (see Table 1). The standard position switching mode with the ‘clean’ reference position 30 arcmin offset from the source in azimuth was used for all observations. Pointing was checked every hour using planets or a known bright source close to the target when planets were not available. Typical on-source time for each source is about 30 minutes. The SIS ALMA Type 1.3mm receiver and Forbes Filter Bank (FFB) backend were employed with two filterbanks configured to 1 MHz (1.38 km s^{-1} at 217.1 GHz) and 250 KHz (0.35 km s^{-1} at 217.1 GHz) spectral resolution sections that provide a bandwidth of about 1000 MHz and 50 MHz, respectively. The FWHM beam size is $\sim 28.5''$ at the observing frequency of 217.1 GHz. Data reduction was undertaken with the CLASS package. We have filtered spectra that show sinusoidal fluctuations, bad baseline and/or strong spikes in some channels. The data were converted from T_A^* to T_{mb} with the beam efficiency of 0.74 measured by the SMT. The typical system temperatures are between 150 and 250 K, and the typical rms noise level ($\delta_{T_{\text{mb}}}$) is about 7 mK at the velocity resolution of 1.38 km s^{-1} . In few cases (5%), the system temperatures reached as high as 350 K due to bad weather conditions.

2.2.3. Infrared bolometric luminosity and dust continuum emission

The infrared bolometric luminosity of our sources is adopted from the Red MSX Source (RMS⁴) survey (Lumsden et al., 2013). The dust continuum emission of our sources at 870 and 850 μm is taken from the ATLASGAL survey (Schuller et al., 2009) and SCUBA Legacy survey (Di Francesco et al., 2008), respectively. These data were used to estimate the gas mass and H_2 column density.

3. RESULTS AND ANALYSIS

The source parameters from the literature are listed in Tables 2 and 3. The WISE 22 μm fluxes retrieved from the WISE archive are listed in column 17. The source temperature estimated from the NH_3 data and its reference are listed in column 18. The source distance, classification, reference and the telescope used are listed in columns 19, 20, 21 and 22 of Table 2, respectively. The sources without SiO 5-4 line detection are summarized in Table 3.

In order to check the consistency between observations of SMT and CSO, we observed W43S and W3(OH) with the SMT and CSO telescopes. Figure 1 shows the comparison of line profiles of the SiO 5-4 transition. The CSO spectra have been resampled to the same spectral resolution of the SMT spectrum. The observed spectra from CSO and SMT observations show similar line profiles. The difference in the velocity integrated intensity between two observations is 8% and 3% for W3(OH) and W43S, respectively. These differences are within the 1σ uncertainty. This suggests that there are no significant discrepancy between the SMT and CSO observations.

3.1. Detection rate

Since the majority of the SiO 5-4 spectra show a non-Gaussian profile (see Figure A1), we used the Full Width at Zero Power (FWZP) velocity range to calculate the integrated intensity (gray in Figure A1), $\int T_{\text{mb}} dv$. The FWZP is visually identified where the emission higher than the 1σ rms noise level. The rms of the velocity integrated intensity is $\sigma_{\text{area}} = \sqrt{N}\sigma\Delta v$, where Δv is the velocity resolution, σ is the rms noise level of spectra, and N is the number of channel within the integrated velocity range. The derived parameters are summarized in Table 2, including the line central velocity (V_{LSR}), velocity integrated intensity ($\int T_{\text{mb}} dv$), line peak brightness temperature (T_{mb}), and FWZP.

The SiO 5-4 emission was detected in 102 out of the 199 sources with velocity integrated intensity above $3\sigma_{\text{area}}$. The detection rate is about 51% for the entire sample. Among them, the SiO 5-4 emission was detected in 25 out of the 44 IRDCs with a detection rate of 57%, 32 out of the 86 protostars with a detection rate of 37%, and 48 out of 69 HII regions with a detection rate of 65%. High detection rate in IRDCs indicates that shock activities are common even in the

² <http://www.iram.fr/IRAMFR/GILDAS>

³ <http://aro.as.arizona.edu/index.htm>

⁴ <http://www.ast.leeds.ac.uk/RMS/>

early evolutionary stage of star formation. The highest detection rate in H_{II} regions indicates that their shocked activities are more common than that in relatively less evolved sources. Even though the CO outflow detection rate is 94% in protostars, they have low detection rate in SiO emission (37%). This could partly due to the fact that the SiO $J = 5 \rightarrow 4$ transition requires a much higher excitation condition than that of the CO low J transitions. On the other hand, we can not rule out that the low detection rate is due to limited sensitivity of observations since the SiO lines emissions are much fainter than the CO lines in these star forming regions.

The large range of source distances from 0.7 to 8.7 kpc in this sample may introduce a bias in the detection rate. In order to examine the effect of distance, we computed the detection rate for 155 sources (44 IRDCs, 62 protostars and 48 H_{II}) as a distance limited sample ($D \leq 4.4$ kpc). The detection rates are 57%, 40% and 63% for IRDCs, protostars, and H_{II} regions, respectively. This is consistent with the results of the whole sample. In addition, we employed the Kolmogorov-Smirnov (KS) test to compare the distance distributions between sources that show detection and non-detection of SiO. The p-value of KS test is a probability that measures the evidence against the null hypothesis. If the p-value is much smaller than 5%, we can reject the null hypothesis that two samples are draw from same parent distribution, while the null hypothesis can not be ruled out if the p-value much larger than 5%. The KS test reveals that the p-value is 46%, 27% and 78% for H_{II} regions, protostars and IRDCs, respectively. This indicates that the distance difference between detection and non-detection sources is no statistically significant for all three categories. Figure 2 shows the cumulative distribution of source distance.

3.2. Line width

Based on the derived FWZP, we divided the SiO spectra into four groups, (1) low-velocity, $\text{FWZP} \leq 10 \text{ km s}^{-1}$; (2) intermediate-velocity, $10 \text{ km s}^{-1} < \text{FWZP} \leq 20 \text{ km s}^{-1}$; (3) high-velocity, $20 \text{ km s}^{-1} < \text{FWZP} \leq 50 \text{ km s}^{-1}$; (4) very high-velocity, $\text{FWZP} > 50 \text{ km s}^{-1}$, similar to the criteria in Beuther & Sridharan (2007). There are nine sources in the low-velocity regime, 43 sources in the intermediate-velocity regime, 47 sources in the high-velocity regime and three sources in the very high-velocity regime. Note that the majority of sources (91%) are associated with $\text{FWZP} > 10 \text{ km s}^{-1}$, which indicates that these SiO emissions arise from gases of relatively high-velocities with respect to the ambient gas velocity. Table 4 lists the number of sources in the four groups for the three categories.

As shown in Figure A1, most of the sources exhibit an asymmetric line profile that can not be fitted by a single Gaussian profile, while some of the sources show extended line wings and 12 sources (05358+3543, G18151-1208MM1, G18151-1208MM2, I18223-1243MM4, G023.60+00.00MM3, G024.33+00.11MM5, S87, ON2S,

G97.53+3.19, 23385+6053, G5.89-0.39 and DR21S) exhibit two distinguishable velocity components. The non-Gaussian extended line wings in the SiO 5-4 emission were detected in 6 out of 25 IRDCs, 12 out of 32 protostars and 14 out of 48 H_{II} regions.

The distributions of FWZP for IRDCs, protostars and H_{II} regions are presented in Figure 3. From these distributions, we note that there are no significant differences between these three categories. The mean FWZP is 20 km s^{-1} , 19 km s^{-1} , and 20 km s^{-1} for IRDCs, protostars, and H_{II} regions, respectively. Furthermore, we derived the median FWZP for all three categories, which is 23 km s^{-1} , 22 km s^{-1} , and 24 km s^{-1} for IRDCs, protostars, and H_{II} regions, respectively. The statistical mean FWZP as well as the median FWZP is similar among different evolutionary stages. Further discussions of relationship between FWZP and evolutionary stages are presented in Section 4.2.

3.3. SiO luminosity

Using the integrated intensity $\int T_{\text{mb}} dv$ and the source distance, we estimated the SiO 5-4 luminosity (L_{SiO}) within the beam (hereafter, luminosity) through (see Nguyen-Lu'o'ng et al., 2013):

$$L_{\text{SiO}} = 4\pi \times d^2 \times \int T_{\text{mb}} dv \\ \simeq 2.3 \times 10^{-4} L_{\odot} \times \left(\frac{d}{6 \text{ kpc}} \right)^2 \frac{\int T_{\text{mb}} dv}{1 \text{ K km s}^{-1}} \quad (1)$$

The derived L_{SiO} is between 1.3×10^{-5} and $1.4 \times 10^{-4} L_{\odot}$ for IRDCs, between 8.5×10^{-7} and $2.5 \times 10^{-4} L_{\odot}$ for protostars, and between 3.6×10^{-6} and $3.7 \times 10^{-3} L_{\odot}$ for H_{II} regions. The mean value is 4.9×10^{-5} , 4.8×10^{-5} and $3.6 \times 10^{-3} L_{\odot}$ for IRDCs, protostars and H_{II} regions, respectively. The median value is 3.8×10^{-5} , 2.3×10^{-5} and $1.3 \times 10^{-4} L_{\odot}$ for IRDCs, protostars and H_{II} regions, respectively. The derived L_{SiO} is summarized in Table 2.

Figure 4 shows distributions of L_{SiO} for the three categories. It is clear that there is a fraction of H_{II} regions (40%) associated with relatively higher L_{SiO} ($> 2.5 \times 10^{-4} L_{\odot}$) than that of IRDCs and protostars. The L_{SiO} of IRDCs is concentrated around $6 \times 10^{-5} L_{\odot}$, while the protostars are distributed throughout between 10^{-6} and $3 \times 10^{-4} L_{\odot}$. We also plotted the L_{SiO} distributions for a distanced limited sample in the right panel of Figure 4, which shows distributions similar to those of the entire sample. There is still a fraction of H_{II} regions (30%) associated with relatively higher L_{SiO} ($> 2.5 \times 10^{-4} L_{\odot}$) in the distance limited sample, which indicates that the high L_{SiO} in H_{II} regions is likely not due to the large distances (see Section 4.3 for a discussion on L_{SiO}).

3.4. SiO column density

Assuming a beam-filling factor of unity and a local thermodynamic equilibrium (LTE) condition for the SiO 5-4 emission, the beam-averaged column density (hereafter, column

density) can be calculated from the velocity integrated intensity $\int T_{\text{mb}} dv$ with the following equation:

$$N = \frac{3h}{8\pi^3 S \mu^2} \frac{Q_{\text{rot}}(T_{\text{ex}})}{g_J g_K g_s} \frac{\exp\left(\frac{E_u}{kT_{\text{ex}}}\right)}{\exp\left(\frac{h\nu}{kT_{\text{ex}}}\right) - 1} \times \frac{1}{J_\nu(T_{\text{ex}}) - J_\nu(T_{\text{bg}})} \frac{1}{1 - \exp(-\tau)} \int T_{\text{mb}} dv \quad (2)$$

where $J_\nu(T) = \frac{h\nu/k}{\exp(h\nu/kT) - 1}$, h is the Planck constant, k is the Boltzmann constant, and T_{ex} and T_{bg} are the excitation temperature of the gas and the temperature of the background radiation, respectively. The line strength $S = J_u/(2J_u + 1)$, the dipole moment $\mu = 3.1$ D for the SiO, line frequency $\nu = 217.104$ GHz, and the upper level energy $E_u/k = 31.26$ K are taken from the splatalogue catalog⁵. The rotational degeneracy g_J is equal to $2J_u + 1$, while the K degeneracy g_K and nuclear spin degeneracy g_s are equal to 1. The partition function $Q_{\text{rot}}(T_{\text{ex}})$ is approximated as $kT_{\text{ex}}/hB + 1/3$, where $B = 21711.967$ MHz is the rotational constant taken from the JPL catalog⁶ (Pickett et al., 1998). Adopting T_{bg} of 2.73 K and assuming that the SiO 5-4 line is optically thin ($\tau \ll 1$), equation (2) can be rewritten as:

$$N(\text{SiO}) = 1.6 \times 10^{11} \text{ cm}^{-2} \times \frac{(T_{\text{ex}} + 0.35) \exp\left(\frac{31.26}{T_{\text{ex}}}\right)}{\exp\left(\frac{10.4}{T_{\text{ex}}}\right) - 1} \frac{1}{J_\nu(T_{\text{ex}}) - J_\nu(T_{\text{bg}})} \int T_{\text{mb}} dv \quad (3)$$

In order to understand the effect of excitation temperatures on the SiO total column density, a wide range of excitation temperatures, from 10 K to 100 K, has been used to calculate the column density. We found that the estimated SiO column densities agree within a factor of two in this temperature range. This indicates that the SiO 5-4 column density does not strongly depend on the temperature, which is consistent with that reported in Nisini et al. (2007). In this paper, we use the kinematic temperatures estimated from the NH₃ data to calculate the SiO column density (Urquhart et al., 2011; Wielen et al., 2012). For sources where the NH₃ measurements are not available, we adopt an excitation temperature T_{ex} of 18 K, 25 K and 30 K for IRDCs, protostars and HII regions, respectively.

The derived SiO column densities range from 2.8×10^{11} to $3.9 \times 10^{12} \text{ cm}^{-2}$ for IRDCs, from 9.6×10^{10} to $4.7 \times 10^{12} \text{ cm}^{-2}$ for protostars, and from 2.4×10^{11} to $2.9 \times 10^{13} \text{ cm}^{-2}$ for HII regions (Table 5). The median and mean column densities are 1.0×10^{12} and $9.0 \times 10^{11} \text{ cm}^{-2}$ for IRDCs, 1.2×10^{12} and 6.1×10^{11} for protostars, and 4.4×10^{12} and $2.2 \times 10^{12} \text{ cm}^{-2}$ for HII regions. The results are comparable to the measurement of SiO column densities toward other massive star

formation regions (e.g., Sakai et al., 2010; Miettinen, 2014; Csengeri et al., 2016). Figure 3 presents the distributions of the SiO column densities for three categories. There are no significant differences between IRDCs and protostars, while the values in HII regions are relatively higher than that in both IRDCs and protostars. The computed SiO column densities are listed in Column 9 of Table 2.

3.5. Gas mass and H₂ column density

We used the emission of dust at 870 or 850 μm retrieved from the ATLASGAL and SCUBA Legacy survey (Schuller et al., 2009; Di Francesco et al., 2008) to estimate the gas mass with the formula:

$$M_{\text{gas}} = \eta \frac{S_\nu d^2}{B_\nu(T) \kappa_\nu} \quad (4)$$

where M_{gas} is the gas mass, $\eta = 100$ is the gas-to-dust ratio, d is the source distance, S_ν is the integrated continuum flux at a frequency of ν , $B_\nu(T)$ is the Planck function at a temperature of T , and κ_ν is the dust opacity at a frequency of ν . We adopt $\kappa_\nu = 10(\nu/1.2 \text{ THz})^\beta \text{ cm}^2 \text{ g}^{-1}$ (Hildebrand, 1983) and assumed $\beta = 1.5$. The derived masses range from 45 up to 17038 M_\odot , which is summarized in Column 15 of Table 2.

We also estimate the peak H₂ column density using the dust emission:

$$N(\text{H}_2) = \eta \frac{F_\nu}{B_\nu(T) \Omega_A \mu_{\text{H}_2} m_{\text{H}} \kappa_\nu} \quad (5)$$

where F_ν is the peak flux density, μ_{H_2} (~ 2.8) is the molecular weight per hydrogen molecule (Kauffmann et al., 2008), m_{H} is the atomic mass unit, Ω_A is the beam solid angle, which is $\Omega_A = (\pi \theta_{\text{HPBW}}^2 / 4 \ln(2))$ for a Gaussian beam. In order to be consistent with the SiO 5-4 data, the dust continuum have been convolved with a beam size of $29''$. The derived H₂ column densities are between 6.4×10^{21} and $6.0 \times 10^{23} \text{ cm}^{-2}$, which are listed in Column 16 of Table 2.

3.6. Bolometric luminosity to mass ratio

The bolometric luminosity-to-mass ratio (L/M) is thought to be a good indicator of the evolutionary stage of star formation. A low L/M value corresponds to an early evolutionary stage of star formation, and vice versa (Molinari et al., 2008). We have retrieved the bolometric luminosity (L_{bol}) from the RMS survey for the sources that show SiO emission (Lumsden et al., 2013). Forty-one HII regions, 26 protostars and 6 IRDCs have bolometric luminosity information (Table 2).

However, the number of IRDCs that have bolometric luminosity measurements is not sufficient for a statistical study. Thus, we included the sources (20 IRDCs, 28 protostars, and 33 HII regions) that have $22 \mu\text{m}$ emission for a statistical study of the properties of SiO in different evolutionary stages (see, e.g., Csengeri et al., 2016). For consistency, we use the WISE $22 \mu\text{m}$ emission to estimate the bolometric luminosity ($L_{\text{bol}}^{22\mu\text{m}}$) with the scaling factor derived by Mottram et al.

⁵ <http://www.cv.nrao.edu/php/splat/>

⁶ <http://spec.jpl.nasa.gov/ftp/pub/catalog/catdir.html>

(2011). The distribution of $L_{\text{bol}}^{22\mu\text{m}}$ is shown in Figure 5. Note that the $L_{\text{bol}}^{22\mu\text{m}}$ tends to be higher in more evolved sources.

Figure 5 shows a comparison of $L_{\text{bol}}^{22\mu\text{m}}$ and L_{bol} , which reveals that both estimations appear to be approximately consistent. The Spearman-rank correlation test, which assesses monotonic relationships, returns a coefficient of 0.48, which indicates that there is a moderate correlation between $L_{\text{bol}}^{22\mu\text{m}}$ and L_{bol} . The $L_{\text{bol}}^{22\mu\text{m}}$ will be used to approximate L_{bol} for estimating the luminosity-to-mass ratio ($L_{\text{bol}}^{22\mu\text{m}}/M$). The derived $L_{\text{bol}}^{22\mu\text{m}}/M$ ranges from 0.03 to 2327, with a mean value of 145. The mean values are 6, 134 and 255 in IRDCs, protostars and HII regions, respectively. The distributions of $L_{\text{bol}}^{22\mu\text{m}}/M$ for the three categories are shown in Figure 5, which reveals that the IRDCs have relatively lower value than that of both protostars and HII regions. We therefore use $L_{\text{bol}}^{22\mu\text{m}}/M$ as an approximate indicator of the evolutionary stage to study the SiO properties as a function of evolutionary stages.

4. DISCUSSIONS

4.1. Uncertainties of the results

The uncertainty in dust continuum flux is typically 10% (Schuller et al., 2009; Di Francesco et al., 2008). The typical uncertainty in the kinematic distances is about 10%, while in some cases it can be orders of magnitudes larger (Reid et al., 2009). Since the gas temperatures estimated from the NH₃ data are not available for the majority of sources, the adopted uniform temperature in Section 3.4 and 3.5 could bring a large uncertainty into the derived parameters. Here, we adopted a conservative uncertainty of 10% for temperature. The η is adopted to be 100 in this study, while its standard deviation is 23 (corresponding to a 1σ uncertainty of 23%) if we assume that it is uniformly distributed between 70 and 150 (Devereux & Young, 1990; Vuong et al., 2003; Sanhueza et al., 2017). We adopted a conservative uncertainty of 28% in κ_v (e.g., Sanhueza et al., 2017). Taking into account these uncertainties, we estimated an uncertainty of 44% and 32% for gas mass and H₂ column density, respectively. However, one has to bear in mind that these uncertainties could be larger.

The errors of the velocity integrated intensities of the SiO emission are estimated with the method described in Section 3.1. Note that the beam dilution effect is expected to affect the measured intensity. This is especially true in our case since the coarse spatial resolution (A beam of 29'' corresponds to 0.56 pc at a distance of 4 kpc) and a fraction of sources (31%) are located at a distance of > 4 kpc. The true beam-filling factor could be smaller than 1 in more distant sources. The derived $N(\text{SiO})$ is at best regarded as the lower limit to the true $N(\text{SiO})$.

4.2. Variations of SiO line widths with evolution

The extended line wings and the broad line width (FWZP > 20 km s⁻¹) of the SiO emission could be due to the high-

velocity gas driven by outflows powered by embedded protostars. Considering that such a line profile is detected in all types of sources, the high-velocity gas related to outflows should be common in various evolutionary stages, from the very early evolutionary stage (i.e., IRDC) to the more evolved (i.e., HII) stage. On the other hand, we can not rule out the fact that these emission features contain contributions from low-velocity shocked gases (e.g., Louvet et al., 2016). We also detected 3 objects with very broad line width (FWZP > 50 km s⁻¹) in the SiO emission (Figure A1), which is likely associated with very high-velocity gas with respect to the ambient gas. There are four sources with two distinguishable velocity components profile in the SiO emission (Figure A1). This emission feature could be produced by two distinctly different velocity outflows, while we can not rule out the other possibilities, e.g., episodic ejection and rotating outflows. These hypotheses can be tested by spatially resolving the kinematics of the SiO emission at higher angular resolutions.

The narrow line width (FWZP < 20 km s⁻¹) in the SiO emission is detected at all three types of sources. This emission could be generated by several processes: (1) small-scale converging flows, such as the case of DR21(OH) (Csengeri et al., 2011) and Cygnus-X (Duarte-Cabral et al., 2014); (2) cloud-cloud collision in molecular clouds, such as the case of massive dense clump W43-MM1/MM2 (Nguyen-Lu'o'ng et al., 2013; Louvet et al., 2016); (3) a population unresolved lower mass protostars (Jiménez-Serra et al., 2010). Since the sources have large mass reservoirs, they have a highly potential to form multiple and/or a group of protostars.

In shock regions, the SiO line widths are dominated by the non-thermal broadening. According to the model by (Gusdorf et al., 2008a), the SiO intensity decreases as the shock passes, and so does the SiO observable line width. At the right panel of Figure 6, we present a plot of FWZP against $L_{\text{bol}}^{22\mu\text{m}}/M$. There is no apparent relationship between FWZP and $L_{\text{bol}}^{22\mu\text{m}}/M$, and its Spearman-rank correlation coefficient is -0.05. We found no significant variations in the line width across the sample, which is similar to the results of Csengeri et al. (2016), who found that the FWZP of the SiO 2-1 line is nearly constant in different evolutionary stages. However, it appears to be in contrary to the results of Sakai et al. (2010) and López-Sepulcre et al. (2011), who reported that the line widths in the early evolutionary phase are broader than that of the more evolved evolutionary phase based on observations of the SiO 2-1 line toward a sample of massive clumps. Since the distance of sources that have $L_{\text{bol}}^{22\mu\text{m}}$ information is comparable to that of Sakai et al. (2010) and López-Sepulcre et al. (2011), it should not be a significant factor for the different results. Several possible reasons can cause such differences: (1) The bias in the sample selection. Both Sakai et al. (2010) (20 sources) and

López-Sepulcre et al. (2011) (57 sources) studies are based on a relatively small sample. (2) This difference could be caused by the different beam sizes because our observations have a relatively large beam ($\sim 29''$) than that of Sakai et al. (2010) ($\sim 18''$) and López-Sepulcre et al. (2011) ($\sim 23''$), which can lead to contamination by nearby sources in our study. Since most of our sources have a mass reservoir higher than $500 M_{\odot}$ within a size of 0.6 pc for a typical distance of 4 kpc, it is highly likely that they form a cluster or multiple sources that produce multiple outflows (Zhang et al., 2015; Wang et al., 2014). In this case, the SiO intensity may not decrease with the evolution of clumps thanks to the efficient SiO replenishment from newly formed outflows/jets. (3) The different could also be due to limited sensitivity of observations for the high velocity line wings.

4.3. Variations of SiO luminosity and abundance with evolution

Figure 7 shows a plot of L_{SiO} against $L_{\text{bol}}^{22\mu\text{m}}/M$. One notes that there is no obvious trend between L_{SiO} and $L_{\text{bol}}^{22\mu\text{m}}/M$, with a correlation coefficient of 0.14 between the two quantities. This indicates that the SiO luminosity does not change significantly for objects at different evolutionary stages, which is consistent with the results of Csengeri et al. (2016). However, this appear to be in contrast with the results by López-Sepulcre et al. (2011), who found a decreasing trend in the SiO luminosity with the evolutionary stage, and it was interpreted as either a decrease in the SiO abundance or a decrease in the jet/outflow energetic with the time evolution of star formation (López-Sepulcre et al., 2011). This discrepancy could be due to the fact that the study of López-Sepulcre et al. (2011) has a relatively narrow range in the L_{SiO} (< 4 orders of magnitude) and L/M (< 4 orders of magnitude) (See also Figure D.2 in Csengeri et al., 2016), while it may also be caused by the bias in the sample selection and/or the different beam sizes (See Section 4.2).

Figure 8 shows a comparison between $N(\text{SiO})$ and $N(\text{H}_2)$. The $N(\text{SiO})$ appears to increase with increasing $N(\text{H}_2)$, with a correlation coefficient of 0.61 between the two quantities. We also find an increasing trend between $N(\text{SiO})$ and M , with a correlation coefficient of 0.43 between the two quantities. These indicate that the column density of SiO increases as a function of dust continuum emission. In order to study the variation of the SiO abundance with evolution, we estimate the SiO abundance $X(\text{SiO}) = N(\text{SiO})/N(\text{N}_2)$. The estimated $X(\text{SiO})$ varies between 1.1×10^{-12} and 2.6×10^{-10} , with a median value of 3.1×10^{-11} and a mean value of 4.0×10^{-11} (Table 5). The derived SiO abundances are comparable to the previous investigations (e.g., Csengeri et al., 2016).

The SiO abundances show no significant differences among three source categories, which have mean and median $X(\text{SiO})$ of around 3×10^{-11} (Table 5). Figure 8 shows a plot of $X(\text{SiO})$ versus to $L_{\text{bol}}^{22\mu\text{m}}/M$. The Spearman-rank correlation test returns a correlation coefficient of 0.19 with a p-value

of 0.15, which confirms that there are not robust trends for the SiO abundances as a function of the evolutionary stage of massive star formation. A similar result has been reported in previous studies, i.e., Sanhueza et al. (2012), Leurini et al. (2014) and Csengeri et al. (2016). If these SiO emissions are due to outflows/jets, the intensity of the outflow/jet would not decrease as massive star formation proceeds. This speculation can be tested through higher angular resolution observations to spatially resolve the SiO emission within these massive clumps.

5. SUMMARY

We used the SMT 10 m and CSO 10.5 m telescopes to observe in the SiO 5-4 line a sample of 185 and 16 massive clumps (two sources were observed in both telescopes), respectively. The sample falls into three different evolutionary stages, IRDCs, protostars and HII regions. Our main results are summarized as follow:

- For a large sample of 199 massive molecular clumps, the SiO 5-4 emission was detected in 102 sources, with a detection rate of 57%, 37%, and 65% for IRDC, protostars, and HII region, respectively. The high detection rate of the SiO emission across all types of sources indicates that the shock activities are common in various evolutionary stages from IRDCs to HII regions. In addition, the presence of the SiO emission in IRDCs implies that there is on-going star formation in most of them.
- Broad line widths and extended non-gaussian line wings are detected among all three evolutionary phases. These emission features are possibly associated with high-velocity shocked gas. We also detected narrow line widths with $\text{FWZP} < 20 \text{ km s}^{-1}$ in all types of sources. They are likely associated with low-velocity gas with respect to the ambient gas. The SiO line widths show no significant differences between three source categories, which indicates that there is no robust trend between the SiO line widths and the evolutionary stages.
- The derived SiO luminosities (L_{SiO}) range from 8.5×10^{-7} to $3.7 \times 10^{-3} L_{\odot}$ for this sample. We do not find any clear trend in the L_{SiO} as a function of the evolutionary stage.
- With the LTE assumption, the derived SiO total column densities are between 9.6×10^{10} and $2.9 \times 10^{13} \text{ cm}^{-2}$. The estimated SiO abundances range from 1.1×10^{-12} to 2.6×10^{-10} , with a mean value of 4.0×10^{-11} . There is no robust trend between the SiO abundance and the evolutionary stage, which suggests that the SiO abundance does not decrease with the advancing evolutionary stage of massive star formation in these massive clumps.

High angular and high sensitivity observations will enable exploration in more detail of SiO outflows at various evolutionary stages of massive star formation.

Facilities: SMT, CSO.

Software: GILDAS (Pety, 2005).

We appreciate the comments from the anonymous referee that helped improving the paper. We are also indebted to the staff at Arizona Radio Observatory for their excellent support in the SMT observations. This work is supported by the National Key R&D Program of China (No. 2017YFA0402704), the Natural Science Foundation of China under grants of 11590783. SL acknowledges support from the CfA pre-doctoral fellowship, the Chinese Scholarship Council, and National Natural Science Foundation of China grant 11629302 and U1731237.

REFERENCES

- Altenhoff, W. J., Downes, D., Pauls, T., & Schraml, J. 1979, *A&AS*, 35, 23
- Arce, H. G., Shepherd, D., Gueth, F., et al. 2007, *Protostars and Planets V*, 245
- Bally, J. 2016, *ARA&A*, 54, 491
- Bergin, E. A., & Tafalla, M. 2007, *ARA&A*, 45, 339
- Beuther, H., Schilke, P., Menten, K. M., et al. 2005, *ApJ*, 633, 535
- Beuther, H., & Sridharan, T. K. 2007, *ApJ*, 668, 348
- Caselli, P., Hartquist, T. W., & Havnes, O. 1997, *A&A*, 322, 296
- Cesaroni, R., Felli, M., Jenness, T., et al. 1999, *A&A*, 345, 949
- Cesaroni, R., Palagi, F., Felli, M., et al. 1988, *A&AS*, 76, 445
- Churchwell, E. 2002, *ARA&A*, 40, 27
- Codella, C., Beltrán, M. T., Cesaroni, R., et al. 2013, *A&A*, 550, A81
- Csengeri, T., Bontemps, S., Schneider, N., et al. 2011, *ApJL*, 740, L5
- Csengeri, T., Leurini, S., Wyrowski, F., et al. 2016, *A&A*, 586, A149
- Devereux, N. A., & Young, J. S. 1990, *ApJ*, 359, 42
- Di Francesco, J., Johnstone, D., Kirk, H., MacKenzie, T., & Ledwosinska, E. 2008, *ApJS*, 175, 277
- Duarte-Cabral, A., Bontemps, S., Motte, F., et al. 2014, *A&A*, 570, A1
- Gerner, T., Beuther, H., Semenov, D., et al. 2014, *A&A*, 563, A97
- Gibb, A. G., & Hoare, M. G. 2007, *MNRAS*, 380, 246
- Griffith, M. R., Wright, A. E., Burke, B. F., & Ekers, R. D. 1994, *ApJS*, 90, 179
- Gusdorf, A., Cabrit, S., Flower, D. R., & Pineau Des Forêts, G. 2008a, *A&A*, 482, 809
- Gusdorf, A., Pineau Des Forêts, G., Cabrit, S., & Flower, D. R. 2008b, *A&A*, 490, 695
- Habing, H. J., & Israel, F. P. 1979, *ARA&A*, 17, 345
- Henshaw, J. D., Caselli, P., Fontani, F., et al. 2013, *MNRAS*, 428, 3425
- Herbst, E., Millar, T. J., Wlodek, S., & Bohme, D. K. 1989, *A&A*, 222, 205
- Hildebrand, R. H. 1983, *QJRAS*, 24, 267
- Jiménez-Serra, I., Caselli, P., Tan, J. C., et al. 2010, *MNRAS*, 406, 187
- Jones, P. A., Burton, M. G., Cunningham, M. R., et al. 2012, *MNRAS*, 419, 2961
- Kauffmann, J., Bertoldi, F., Bourke, T. L., Evans, II, N. J., & Lee, C. W. 2008, *A&A*, 487, 993
- Le Picard, S. D., Canosa, A., Pineau des Forêts, G., Rebrion-Rowe, C., & Rowe, B. R. 2001, *A&A*, 372, 1064
- Lesaffre, P., Pineau des Forêts, G., Godard, B., et al. 2013, *A&A*, 550, A106
- Leurini, S., Codella, C., Gusdorf, A., et al. 2013, *A&A*, 554, A35
- Leurini, S., Codella, C., López-Sepulcre, A., et al. 2014, *A&A*, 570, A49
- Li, J., Wang, J., Zhu, Q., Zhang, J., & Li, D. 2015, *ApJ*, 802, 40
- Li, S., Wang, J., Zhang, Z.-Y., et al. 2017, *MNRAS*, 466, 248
- López-Sepulcre, A., Walmsley, C. M., Cesaroni, R., et al. 2011, *A&A*, 526, L2
- Louvet, F., Motte, F., Gusdorf, A., et al. 2016, *A&A*, 595, A122
- Lumsden, S. L., Hoare, M. G., Urquhart, J. S., et al. 2013, *ApJS*, 208, 11
- Mac Low, M.-M., & Klessen, R. S. 2004, *Reviews of Modern Physics*, 76, 125
- Martin-Pintado, J., Bachiller, R., & Fuente, A. 1992, *A&A*, 254, 315
- Martin-Pintado, J., de Vicente, P., Fuente, A., & Planesas, P. 1997, *ApJL*, 482, L45
- Maršálková, P. 1974, *Ap&SS*, 27, 3
- Maud, L. T., Lumsden, S. L., Moore, T. J. T., et al. 2015a, *MNRAS*, 452, 637
- Maud, L. T., Moore, T. J. T., Lumsden, S. L., et al. 2015b, *MNRAS*, 453, 645
- Maud, L. T., Cesaroni, R., Kumar, M. S. N., et al. 2018, *A&A*, 620, A31
- McKee, C. F., & Ostriker, E. C. 2007, *ARA&A*, 45, 565
- Miettinen, O. 2014, *A&A*, 562, A3
- Miettinen, O., Harju, J., Haikala, L. K., & Pomrnén, C. 2006, *A&A*, 460, 721
- Molinari, S., Pezzuto, S., Cesaroni, R., et al. 2008, *A&A*, 481, 345
- Motte, F., Bontemps, S., & Louvet, F. 2018, *ARA&A*, 56, 41
- Motte, F., Bontemps, S., Schilke, P., et al. 2007, *A&A*, 476, 1243
- Mottram, J. C., Hoare, M. G., Urquhart, J. S., et al. 2011, *A&A*, 525, A149
- Nguyen-Lu'ong, Q., Motte, F., Carlhoff, P., et al. 2013, *ApJ*, 775, 88
- Nisini, B., Codella, C., Giannini, T., et al. 2007, *A&A*, 462, 163
- Pety, J. 2005, in *SF2A-2005: Semaine de l'Astrophysique Francaise*, ed. F. Casoli, T. Contini, J. M. Hameury, & L. Pagani, 721
- Pickett, H. M., Poynter, R. L., Cohen, E. A., et al. 1998, *JQSRT*, 60, 883
- Pillai, T., Kauffmann, J., Wyrowski, F., et al. 2011, *A&A*, 530, A118
- Pillai, T., Wyrowski, F., Carey, S. J., & Menten, K. M. 2006, *A&A*, 450, 569
- Qiu, K., Zhang, Q., Beuther, H., & Yang, J. 2007, *ApJ*, 654, 361
- Reid, M. J., Menten, K. M., Zheng, X. W., et al. 2009, *ApJ*, 700, 137
- Reid, M. J., Menten, K. M., Brunthaler, A., et al. 2014, *ApJ*, 783, 130
- Rivero-Santamaría, A., Dayou, F., Rubayo-Soneira, J., & Monnerville, M. 2014, *Chemical Physics Letters*, 610, 335
- Sakai, T., Sakai, N., Hirota, T., & Yamamoto, S. 2010, *ApJ*, 714, 1658
- Sakai, T., Sakai, N., Kamegai, K., et al. 2008, *ApJ*, 678, 1049
- Sánchez-Monge, Á., López-Sepulcre, A., Cesaroni, R., et al. 2013, *A&A*, 557, A94
- Sanhueza, P., Jackson, J. M., Foster, J. B., et al. 2012, *ApJ*, 756, 60
- Sanhueza, P., Jackson, J. M., Zhang, Q., et al. 2017, *ApJ*, 841, 97
- Schilke, P., Walmsley, C. M., Pineau des Forêts, G., & Flower, D. R. 1997, *A&A*, 321, 293
- Schuller, F., Menten, K. M., Contreras, Y., et al. 2009, *A&A*, 504, 415
- Shirley, Y. L., Evans, II, N. J., Young, K. E., Knez, C., & Jaffe, D. T. 2003, *ApJS*, 149, 375
- Sridharan, T. K., Beuther, H., Schilke, P., Menten, K. M., & Wyrowski, F. 2002, *ApJ*, 566, 931
- Urquhart, J. S., Morgan, L. K., Figura, C. C., et al. 2011, *MNRAS*, 418, 1689
- Vuong, M. H., Montmerle, T., Grosso, N., et al. 2003, *A&A*, 408, 581
- Wang, K., Zhang, Q., Testi, L., et al. 2014, *MNRAS*, 439, 3275
- Wienen, M., Wyrowski, F., Schuller, F., et al. 2012, *A&A*, 544, A146
- Wright, A. E., Griffith, M. R., Burke, B. F., & Ekers, R. D. 1994, *ApJS*, 91, 111
- Zhang, Q., Hunter, T. R., Brand, J., et al. 2005, *ApJ*, 625, 864
- Zhang, Q., Hunter, T. R., Sridharan, T. K., & Cesaroni, R. 1999, *ApJL*, 527, L117
- Zhang, Q., Wang, K., Lu, X., & Jiménez-Serra, I. 2015, *ApJ*, 804, 141

Zinnecker, H., & Yorke, H. W. 2007, *Annual Review of Astronomy and Astrophysics*, 45, 481

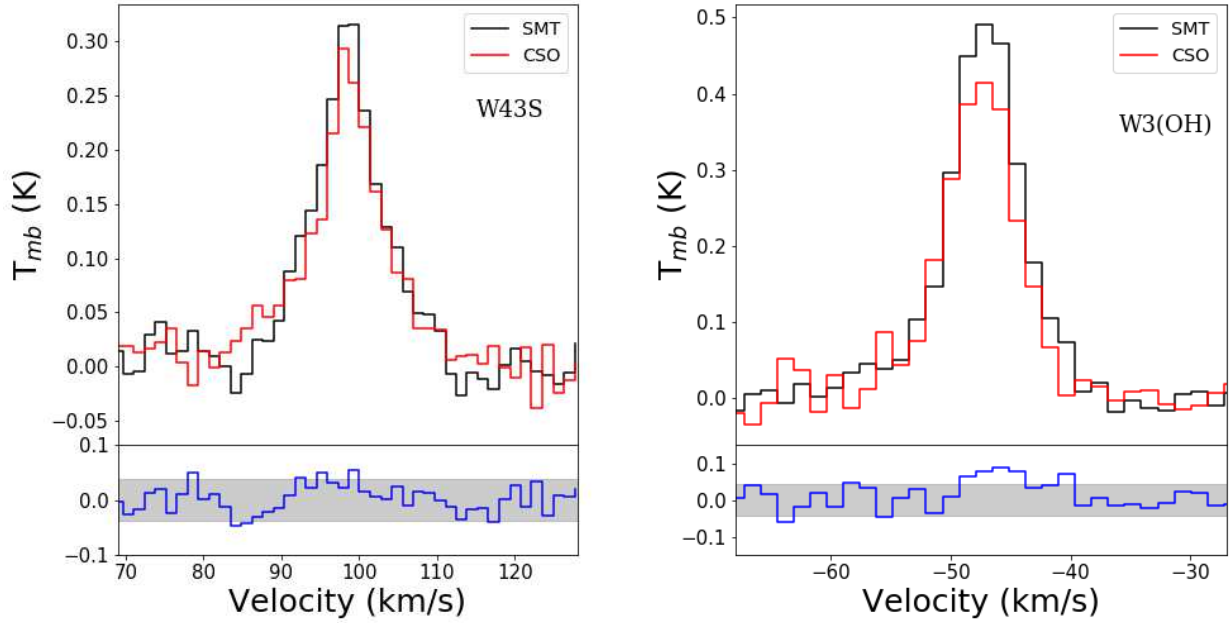


Figure 1. Spectral lines of the SiO 5-4 transition (black and red histograms) obtained from the observations with the SMT and CSO telescopes, respectively. The bottom panels show the residuals after the SMT data being subtracted by the CSO data, while the gray shadow shows the rms level of the spectral line observed by the CSO. The spectral line data from the CSO are re-sample to 1.38 km s^{-1} , the same spectral resolution of the SMT. *Left:* The spectra of the SiO 5-4 line in W43S. *Right:* The spectra of the SiO 5-4 line in W3(OH).

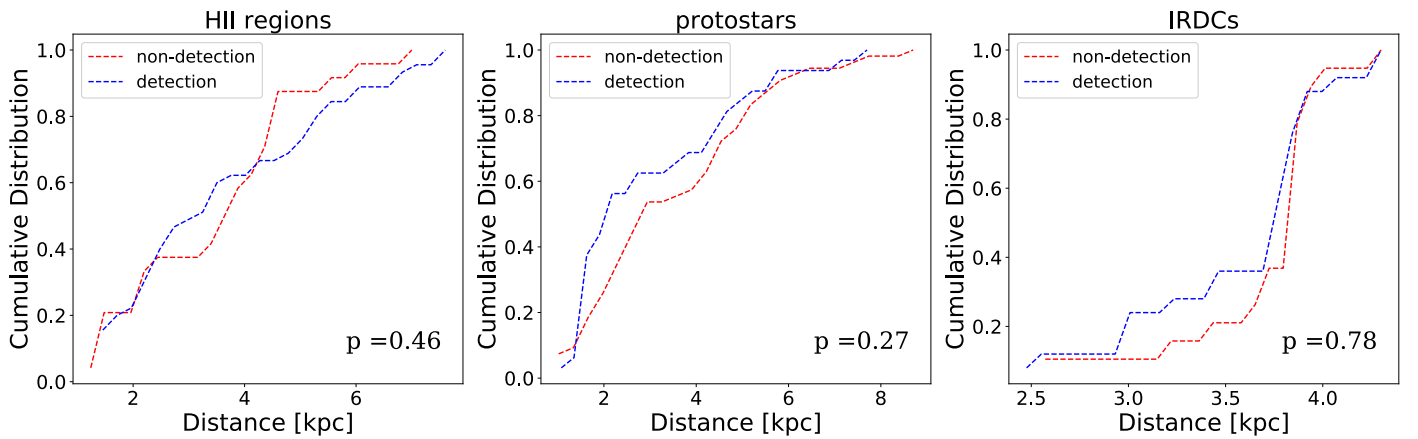


Figure 2. Distance distributions for sources with and without SiO detections (The blue and red dash lines). From *left to right* are HII regions, protostars and IRDCs. The p -value from the KS test is presented inside the panel.

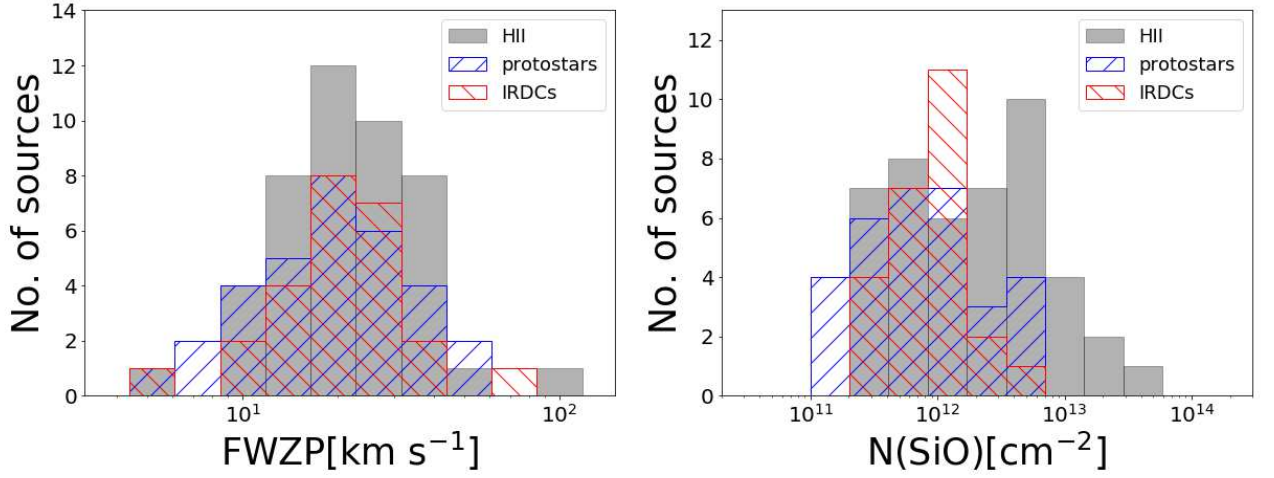


Figure 3. *Left:* Histograms showing the FWZP distributions for HII regions (gray), protostars (blue), and IRDCs (red). *Right:* Same as left but for SiO column density distributions.

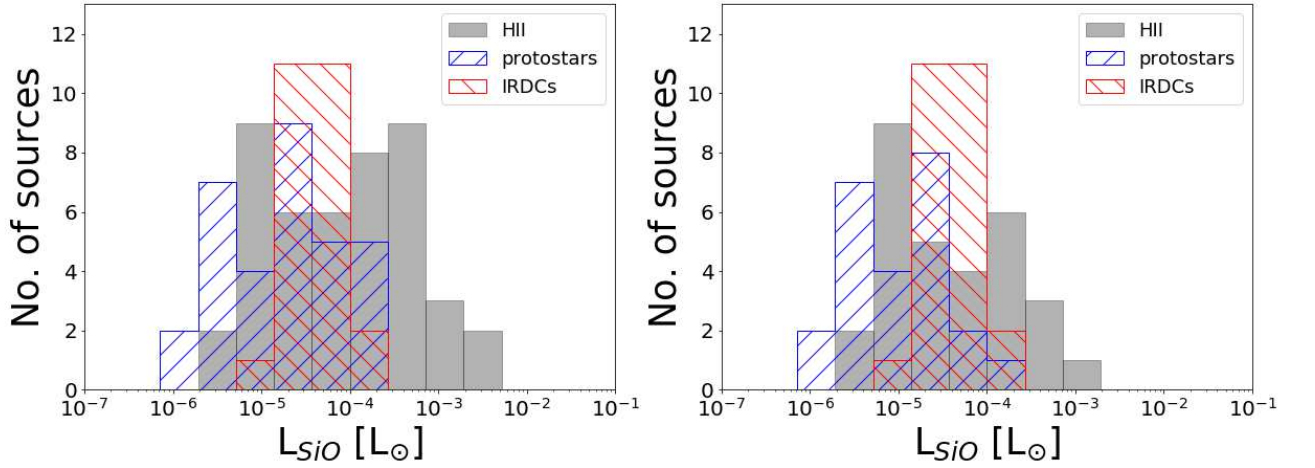


Figure 4. *Left:* Histograms showing the L_{SiO} distributions of IRDCs (red), protostars (blue) and HII regions (black). *Right:* Same as left but for distance limited samples.

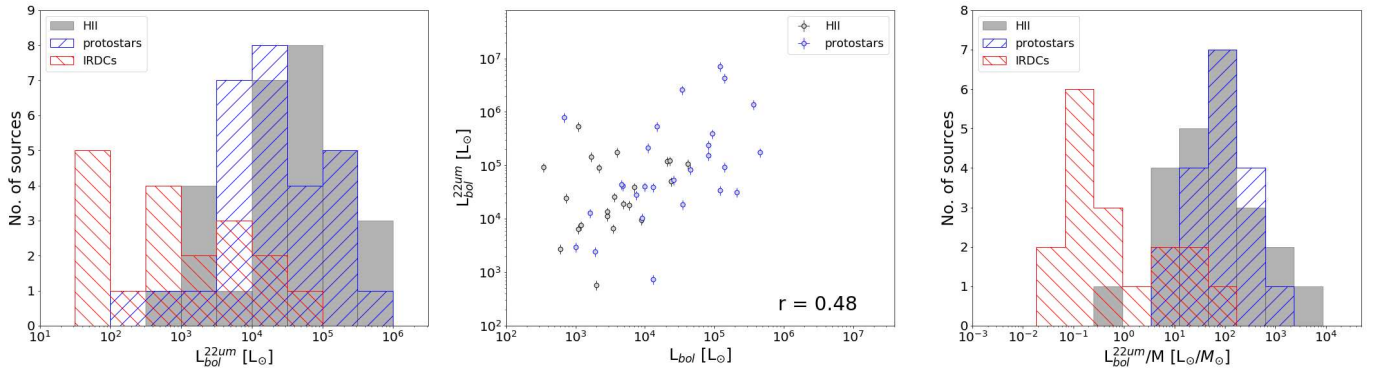


Figure 5. *Left:* Histograms are the distributions of bolometric luminosity derived from WISE 22 μm for three categories. *Middle:* The bolometric luminosity derived from WISE WISE 22 μm versus bolometric luminosity derived by SED fitting. Blue and gray circles represent protostars and HII regions, respectively. *Right:* Histograms are the distributions of L_{bol}^{22μm}/M for three categories.

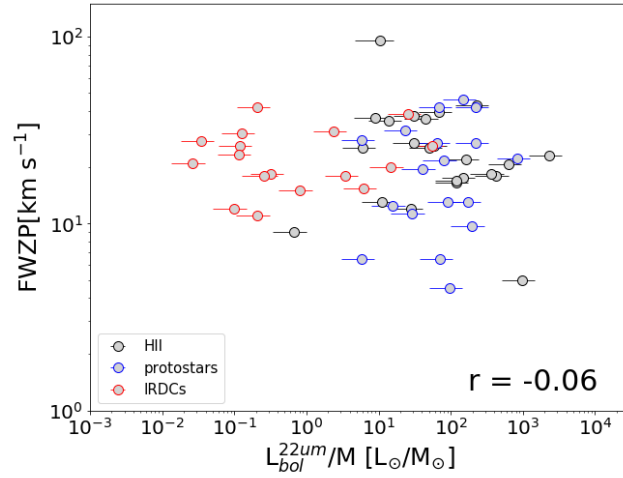


Figure 6. The FWZP of the SiO 5-4 line versus the source luminosity-to-mass ratio. The grey, blue and red circles represent HII regions, protostars and IRDCs, respectively. The coefficient from the Spearman-rank correlation test is presented inside the panel.

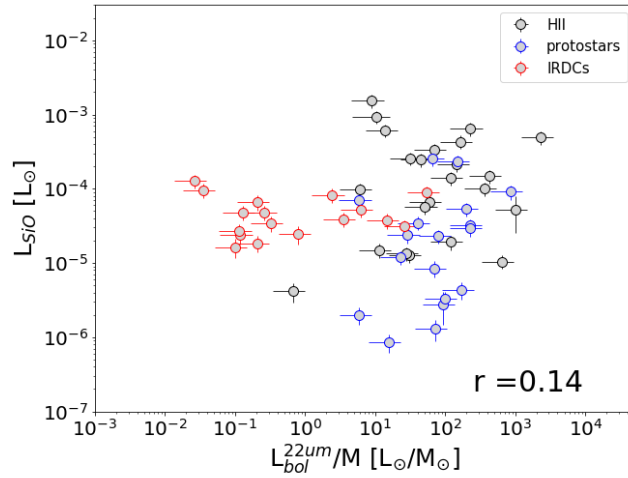


Figure 7. The SiO 5-4 luminosity versus the luminosity-to-mass ratio. The grey, blue and red circle are HII regions, protostars and IRDCs, respectively. The coefficient from the Spearman-rank correlation test is presented inside the panel.

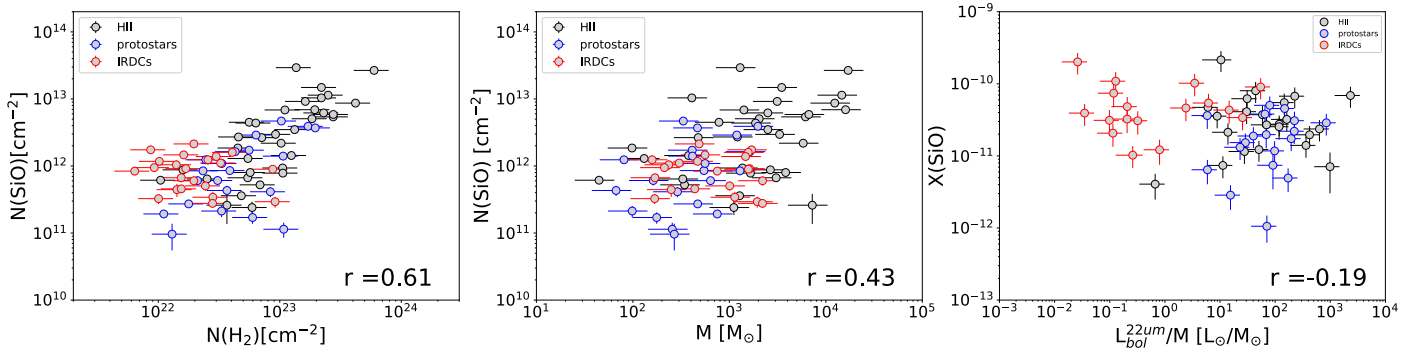


Figure 8. *Left:* SiO column density versus H₂ beam-averaged column density. *Middle:* The SiO column density versus gas mass. *Right:* SiO abundance versus luminosity-to-mass ratio. The grey, blue and red circle are HII regions, protostars and IRDCs, respectively. The coefficient from the Spearman-rank correlation test is presented inside the panel.

Table 1. Summary of observations

Telescope–Instrument	Date	Spectra resolution	θ_{beam}	No. of sources
SMT 10 m	2015	1MHz/0.25Mhz (1.38 km s ⁻¹ /0.35 km s ⁻¹)	~ 28.5''	88
SMT 10 m	2016	1MHz/0.25Mhz (1.38 km s ⁻¹ /0.35 km s ⁻¹)	~ 28.5''	97
CSO 10.4 m	2013	0.27MHz (0.37 km s ⁻¹)	~ 27.4''	16

Table 4. The SiO 5-4 line widths.

Source groups	total	FWZP ≤ 10 km s ⁻¹	10 < FWZP ≤ 20 km s ⁻¹	20 < FWZP ≤ 50 km s ⁻¹	FWZP > 50 km s ⁻¹	median FWZP km s ⁻¹	mean FWZP km s ⁻¹
IRDCs	25	1	12	11	1	20	23
protostars	32	5	12	14	1	19	22
HII	45	3	19	22	1	20	24

Table 5. The SiO column densities and abundances.

Source groups	$N(\text{SiO})_{\min}$ (cm ⁻²)	$N(\text{SiO})_{\max}$ (cm ⁻²)	$N(\text{SiO})_{\text{average}}$ (cm ⁻²)	$N(\text{SiO})_{\text{median}}$ (cm ⁻²)	$X(\text{SiO})_{\text{average}}$	$X(\text{SiO})_{\text{median}}$
IRDCs	2.8×10^{11}	3.9×10^{12}	1.0×10^{12}	9.0×10^{11}	5.8×10^{-11}	4.1×10^{-11}
protostars	9.6×10^{10}	4.7×10^{12}	1.2×10^{12}	6.1×10^{11}	2.3×10^{-11}	2.0×10^{-11}
HII	2.4×10^{11}	2.9×10^{13}	4.4×10^{12}	2.2×10^{12}	3.8×10^{-11}	2.7×10^{-11}
All sources	9.6×10^{10}	2.9×10^{13}	2.5×10^{12}	9.3×10^{11}	4.0×10^{-11}	3.1×10^{-11}

Table 2. SiO 5-4 line parameters and source properties.

No	Name	R.A J2000	Dec J2000	$\int T_{\text{mb}} dv$ K km s ⁻¹	v_{lsr} km s ⁻¹	T_{mb} K	FWZP km s ⁻¹	$N(\text{SiO})$ cm ⁻²	L_{SiO} L _⊙	L_{bol} L _⊙	F_{ν} Jy beam ⁻¹	S_{ν} Jy	λ μm	M_{gas} M _⊙	$N(\text{H}_2)$ cm ⁻²	$S_{22\mu\text{m}}$ Jy	T_{k} K	D kpc	Type	Ref	Telescope
1	G121.30+0.66	00:36:47.5	+63:29:02	1.39±0.07	-17.2±0.1	0.26	27	1.85E+12	1.28E-05	1.00E+03	6.45	19.32	850	98	4.52E+22	17.2±0.16	...	1.2	HII	1	SMT
2	G123.07-6.31	00:52:25.2	+56:33:53	1.89±0.09	-30.9±0.2	0.25	22.5	2.52E+12	5.84E-05	2.03±0.06	...	2.2	HII	1	SMT	
3	G133.6945+01.2166	02:25:30.0	+62:06:20	0.7±0.07	-44±0.4	0.1	13	9.34E+11	1.79E-05	1.20E+04	15.06	97.04	850	1367	1.06E+23	...	2	HII	3	SMT	
4	G133.7150+01.2155	02:25:40.0	+62:05:52	2.84±0.11	-38.9±0.1	0.39	25	3.91E+12	7.26E-05	1.40E+05	19.11	109.95	850	1977	1.71E+23	...	2	protostar	3	SMT	
5	W3(OH)	02:27:04.6	+61:52:25	3.8±0.09	-47.3±0.1	0.49	16.5	5.07E+12	1.40E-04	8.30E+04	26.29	100.56	850	2039	1.84E+23	349.17±1.61	...	2.4	UCHII	1	SMT
	W3(OH)	02:27:04.6	+61:52:25	3.47±0.10	-48.2±0.2	0.48	17.0	4.62E+12	1.28E-04	8.30E+04	26.29	100.56	850	2039	1.84E+23	349.17±1.61	...	2.4	UCHII	1	CSO
6	G135.28+2.80	02:43:29.1	+62:56:59	0.46±0.05	-72.6±1.3	0.03	42.5	6.14E+11	1.69E-05	2.90E+04	1.49	2.2	850	45	1.04E+22	...	2.4	UCHII	1	SMT	
7	05137+3919	05:17:13.3	+39:22:14	0.14±0.01	-29.4±0.5	0.03	9.7	1.93E+11	5.30E-05	1.70E+03	1.24	2.81	850	749	1.11E+22	20.56±0.15	...	7.7	protostar	4	SMT
8	05274+3345	05:30:45.6	+33:47:52	0.08±0.02	-3.7±0.5	0.03	6.5	1.14E+11	1.31E-06	5.90E+03	10.46	19.3	850	256	1.08E+23	58.92±0.05	22.6	1.6	protostar	4	SMT
9	05358+3543	05:39:10.4	+35:45:19	0.41±0.06	-16.1±1.6	0.03	42	6.08E+11	8.49E-06	2.90E+03	2.65	8.6	850	163	3.08E+22	28.78±0.11	20.8	1.8	protostar	5	SMT
10	S231	05:39:12.9	+35:45:54	1.94±0.07	-17.1±0.1	0.25	26	2.65E+12	6.56E-05	7.60E+03	8.25	20.77	850	476	7.11E+22	44.12±0.08	25.7	2.3	HII	1	SMT
11	05373+2349	05:40:24.4	+23:50:54	0.9±0.06	2.5±0.4	0.09	21.7	1.24E+12	2.30E-05	1.10E+03	2.75	4.5	850	81	2.46E+22	13.45±0.16	...	2	protostar	4	SMT
12	S235	05:40:53.3	+35:41:49	0.36±0.03	-17.5±0.2	0.08	10	5.23E+11	5.89E-06	5.30E+03	6.26	24.27	850	343	6.88E+22	...	21.6	1.6	HII	1	SMT
13	S241	06:03:53.6	+30:14:44	0.24±0.04	-7.9±0.6	0.04	12.5	3.20E+11	3.39E-05	1.47±0.03	...	4.7	HII	1	SMT	
14	S252A	06:08:35.4	+20:39:03	0.41±0.03	9.9±0.1	0.09	10.5	5.47E+11	5.89E-06	8.71±0.2	...	1.5	HII	1	SMT	
15	06056+2131	06:08:41.0	+21:31:01	0.3±0.05	2.5±0.5	0.05	13	4.13E+11	4.31E-06	2.40E+04	9.35	28.63	850	290	8.37E+22	184.26±0.34	...	1.5	protostar	4	SMT
16	S255	06:12:53.7	+17:59:22	0.97±0.07	7.7±0.3	0.12	20.9	1.29E+12	1.05E-05	4.50E+04	7.81	22.01	850	131	5.47E+22	410.62±0.76	...	1.3	UCHII	1	SMT
17	G194.9259-01.1946	06:13:21.0	+15:23:57	0.29±0.04	-5.2±0.7	0.04	15.5	3.87E+11	7.41E-06	1.60E+03	26.56±0.42	...	2	HII	3	SMT	
18	G5.89-0.39	18:00:30.3	-24:04:00	21.52±0.31	15.4±0.2	0.76	96	2.93E+13	9.29E-04	...	25.73	71.84	870	1294	1.36E+23	16.57±4.16	39.7	2.6	UCHII	2	CSO
19	G10.6-0.4	18:10:28.7	-19:55:48	8.54±0.11	-3.5±0.1	0.96	23.3	1.14E+13	1.96E-03	3.90E+05	33.1	107.17	870	14630	2.50E+23	...	6	CHII	1	CSO	
20	G11.94-0.62	18:14:01.1	-18:53:24	0.5±0.02	38.8±0.4	0.05	25.5	6.67E+11	5.64E-05	8.30E+04	7.22	45.64	870	3053	5.45E+22	73.22±1.28	...	4.2	UCHII	2	CSO
21	W33IRS3	18:14:13.3	-17:55:40	4.05±0.13	35.8±0.1	0.51	18	5.40E+12	1.49E-04	3.40E+04	36.48	281.79	870	6155	2.75E+23	3744.9	...	2.4	CHII	2	CSO
22	I18151-1208MM2	18:17:50.0	-12:07:55	2.37±0.15	29.6±0.7	0.09	68.5	3.86E+12	1.36E-04	1.12±0.05	...	3	IRDC	6	SMT	
23	G015.05+00.07MM1	18:17:50.0	-15:53:38	0.25±0.05	25.4±0.2	0.06	12	4.44E+11	1.64E-05	...	0.79	2.69	870	249	1.42E+22	0.02	16.31	3.2	IRDC	6	SMT
24	I18151-1208MM3	18:17:52.0	-12:06:56	0.28±0.03	32.6±0.5	0.05	19	4.56E+11	1.61E-05	6.53±0.13	...	3	IRDC	6	SMT	
25	I18151-1208MM1	18:17:58.0	-12:07:27	0.49±0.07	34.2±0.5	0.08	19	7.98E+11	2.82E-05	2.20E+04	79.26±1.31	...	3	IRDC	6	SMT	
26	I18182-1433MM1	18:21:09.0	-14:31:57	1.03±0.05	60±0.3	0.11	26	1.47E+12	9.01E-05	...	1.47	7.38	870	560	1.62E+22	18.56±0.24	22.67	3.7	IRDC	6	SMT
27	I18223-1243MM4	18:25:07.0	-12:47:54	0.76±0.11	46.9±1.6	0.05	42	1.24E+12	6.65E-05	...	1.66	1.49	870	158	2.57E+22	0.02	...	3.7	IRDC	6	SMT
28	I18223-1243MM3	18:25:08.0	-12:45:28	0.53±0.06	45±0.3	0.08	20.5	8.38E+11	4.64E-05	...	0.44	7.49	870	750	6.40E+21	...	18.73	3.7	IRDC	6	SMT
29	G019.27+00.07MM2	18:25:53.0	-12:04:48	0.64±0.09	26.5±1.2	0.04	26	1.04E+12	2.36E-05	...	0.91	5.26	870	235	1.41E+22	0.04	...	2.4	IRDC	6	SMT
30	G019.27+00.07MM1	18:25:58.0	-12:03:59	1.31±0.1	26.5±0.6	0.13	30.5	2.13E+12	4.82E-05	...	1.27	10.86	870	486	1.96E+22	0.09	...	2.4	IRDC	6	SMT
31	G19.61-0.23	18:27:38.0	-11:56:28	4.24±0.19	40.8±0.3	0.3	39.5	6.19E+12	3.32E-04	4.60E+05	19.2	34	870	2504	2.30E+23	118.64±1.09	21.4	3.5	CHIII	1	SMT
32	G20.08-0.13	18:28:10.0	-11:28:48	3.37±0.18	42.6±0.4	0.25	36.5	4.49E+12	2.49E-04	1.20E+05	7.68	18.43	870	781	5.60E+22	24.88±0.34	30.8	3.4	UCHII	1	SMT

$\int T_{\text{mb}} dv$: velocity integrated intensity. v_{lsr} : line central velocity. T_{mb} : emission peak at main beam temperature. FWZP: line width – Full Widths at Zero Power. $N(\text{SiO})$: beam-averaged total column density of SiO. L_{SiO} : beam-averaged luminosity of SiO 5-4 line. L_{bol} : source bolometric luminosity. F_{ν} : peak flux density of dust continuum. S_{ν} : integrated intensity of dust continuum. λ : wavelength of dust continuum. M_{gas} : gas mass. $N(\text{H}_2)$: H₂ total column density. $S_{22\mu\text{m}}$: source flux at WISE 22 μm. T_{k} : temperature derived from the NH₃ data. D: source distance. Type: source classification. Ref: reference.

Reference – (1) Shirley et al. (2003); (2) Li et al. (2015); (3) Maud et al. (2015b); (4) Zhang et al. (2005); (5) Sridharan et al. (2002); (6) Sakai et al. (2008).

No	Name	R.A J2000	Dec J2000	$\int T_{\text{mb}} dv$ K km s ⁻¹	v_{LSR} km s ⁻¹	T_{mb} K	FWZP km s ⁻¹	$N(\text{SiO})$ cm ⁻²	L_{SiO} L _⊙	L_{bol} L _⊙	F_{ν} Jy beam ⁻¹	S_{ν} Jy	λ μm	M_{gas} M _⊙	$N(\text{H}_2)$ cm ⁻²	$S_{22\mu\text{m}}$ Jy	T_{k} K	D kpc	Type	Ref	Telescope
33	G022.35+00.41MM2	18:30:24.0	-09:12:44	0.21±0.04	51.2±0.5	0.03	15	3.42E+11	2.48E-05	...	1.82	7.92	870	1137	2.81E+22	0.41±0.02	...	4.3	IRDC	6	SMT
34	G022.35+00.41MM1	18:30:24.0	-09:10:34	1.07±0.03	52.1±0.2	0.13	21	1.74E+12	1.26E-04	...	0.56	11.84	870	1700	8.66E+21	0.02	...	4.3	IRDC	6	SMT
35	118306-0835MM1	18:33:24.0	-08:33:31	0.78±0.06	80.6±0.7	0.05	38.5	1.11E+12	3.11E-05	1.00E+04	2.98	8.8	870	302	3.26E+22	10.32±0.31	22.8	2.5	IRDC	6	SMT
36	G023.60+00.00MM3	18:34:10.0	-08:18:28	0.28±0.03	96.7±0.4	0.03	15	4.56E+11	2.72E-05	1.10E+04	1	3.71	870	438	1.55E+22	3.9	IRDC	6	SMT
37	G023.60+00.00MM1	18:34:12.0	-08:19:06	0.98±0.07	107.2±0.6	0.1	27.5	1.60E+12	9.52E-05	...	2.63	13.28	870	1569	4.07E+22	0.03	...	3.9	IRDC	6	SMT
38	G023.60+00.00MM2	18:34:21.0	-08:18:07	0.85±0.08	51.7±0.8	0.06	31	1.38E+12	8.26E-05	...	1.94	12.46	870	1472	3.00E+22	1.94±0.08	...	3.9	IRDC	6	SMT
39	G024.33+00.11MM1	18:35:08.0	-07:35:04	0.56±0.04	114±0.5	0.09	15.5	9.12E+11	5.17E-05	...	1.09	14.46	870	1622	1.68E+22	5.78±0.11	...	3.8	IRDC	6	SMT
40	G024.33+00.11MM8	18:35:23.0	-07:37:21	0.18±0.03	95.5±0.6	0.04	10.5	2.93E+11	1.66E-05	...	5.92	17.38	870	1949	9.15E+22	3.8	IRDC	6	SMT
41	G024.33+00.11MM3	18:35:28.0	-07:36:18	0.37±0.05	117.7±0.3	0.05	18.5	6.03E+11	3.41E-05	...	1.27	19.69	870	2208	1.96E+22	0.41±0.01	...	3.8	IRDC	6	SMT
42	G024.33+00.11MM2	18:35:34.0	-07:37:28	0.2±0.03	119.3±0.6	0.04	11	3.26E+11	1.85E-05	...	0.65	1.5	870	168	1.00E+22	0.02	...	3.8	IRDC	6	SMT
43	G024.33+00.11MM5	18:35:34.0	-07:36:42	0.41±0.05	115.5±0.3	0.05	20	6.68E+11	3.78E-05	...	1	1.51	870	169	1.55E+22	1.43±0.03	...	3.8	IRDC	6	SMT
44	G024.60+00.08MM2	18:35:36.0	-07:18:09	0.31±0.04	115.5±0.6	0.04	23.5	5.05E+11	2.71E-05	...	1.58	9.48	870	1008	2.44E+22	0.07	...	3.7	IRDC	6	SMT
45	G024.60+00.08MM1	18:35:40.0	-07:18:37	0.55±0.04	53.6±0.3	0.07	18	8.96E+11	4.81E-05	...	5.66	14.82	870	1576	8.75E+22	0.25±0.04	...	3.7	IRDC	6	SMT
46	G24.49-0.04	18:36:05.3	-07:31:23	3.41±0.17	110.1±0.6	0.21	47	4.55E+12	2.67E-04	2.10E+05	21.33±0.33	...	3.5	HII	1	SMT
47	118337-0743MM3	18:36:18.0	-07:41:01	0.72±0.05	55.5±0.6	0.06	31	1.17E+12	7.36E-05	...	0.66	3.77	870	468	1.02E+22	4	IRDC	6	SMT
48	G025.04-00.20MM1	18:38:10.0	-07:02:34	0.53±0.04	61.5±0.7	0.08	18	9.45E+11	3.91E-05	...	0.51	2.01	870	212	9.27E+21	0.53±0.02	16.23	3.4	IRDC	6	SMT
49	G025.04-00.20MM4	18:38:14.0	-07:03:12	0.17±0.02	65.8±0.2	0.07	6	2.77E+11	1.26E-05	...	1.81	24.55	870	2204	2.80E+22	3.4	IRDC	6	SMT
50	G28.86+0.07	18:43:46.0	-03:35:36	0.61±0.05	106±0.9	0.08	17.5	8.76E+11	2.13E-04	9.40E+04	3.82	23.13	870	2660	1.60E+22	59.19±0.33	48.4	7.4	HII	1	SMT
51	W43S	18:46:04.0	-02:39:26	3.21±0.15	97.8±0.2	0.35	23	4.37E+12	4.92E-04	1.40E+05	12.01	29.3	870	1869	6.35E+22	1506.05±4.16	39.8	4.9	UCHII	1	SMT
	W43S	18:46:04.0	-02:39:26	3.11±0.12	97.9±0.3	0.34	24.0	4.22E+12	4.77E-04	1.40E+05	12.01	29.3	870	1869	6.35E+22	1506.05±4.16	39.8	4.9	UCHII	1	CSO
52	G31.41+0.31	18:47:35.0	-01:12:46	4±0.19	97.1±0.3	0.35	35.5	5.87E+12	6.14E-04	1.40E+05	22.74	45.61	870	6672	2.76E+23	32.23±0.33	21.2	4.9	UCHII	1	SMT
53	W43Main3	18:47:47.0	-01:54:35	5.18±0.16	98.9±0.2	0.46	37	6.91E+12	1.53E-03	...	25.72	91.37	870	16021	1.94E+23	25.6	...	6.8	HII	1	SMT
54	G34.26+0.15	18:53:18.5	+01:14:57	6.5±0.21	59.3±0.1	0.93	19.5	8.67E+12	5.69E-04	...	55.65	238.32	870	12372	4.20E+23	3.7	UCHII	2	CSO
55	G35.20-0.74	18:58:12.7	+01:40:36	0.58±0.06	33±0.3	0.12	13	7.83E+11	1.48E-05	3.50E+04	12.35	95.8	870	1653	1.06E+23	38.78±1.11	27.2	2	HII	1	CSO
56	G45.45+0.06	19:14:21.3	+11:09:12	0.19±0.09	-51.2±0.3	0.08	5	2.60E+11	5.29E-05	1.20E+05	3.9	35.12	870	7239	3.67E+22	1368.49±3.78	25.4	6.6	UCHII	2	CSO
57	W51W	19:23:11.0	+14:26:38	0.6±0.04	52.1±0.3	0.08	18.5	7.99E+11	9.97E-05	3.70E+05	8.62	44.26	870	3832	5.71E+22	444.47	33.2	5.1	HII	1	CSO
58	W51D	19:23:39.9	+14:31:06	6.26±0.31	60.8±0.2	0.71	23	9.19E+12	1.04E-03	5.20E+04	41.67	61.54	870	3132	1.62E+23	...	51.4	5.1	UCHII	2	CSO
59	W51M	19:23:43.8	+14:30:29	19.99±0.52	56.6±0.1	1.68	25.5	2.67E+13	3.32E-03	5.10E+05	79.14	172.74	870	17038	5.97E+23	5.1	CHII	1	SMT
60	19368+2239	19:38:58.1	+22:46:32	0.57±0.07	36.6±0.5	0.07	28	8.47E+11	7.05E-05	1.20E+03	1.86	10.57	870	1291	2.33E+22	3.26±0.04	20.7	4.4	protostar	4	SMT
61	19388+2357	19:40:59.4	+24:04:39	0.2±0.02	34.2±0.5	0.03	11.3	2.72E+11	2.36E-05	2.90E+03	1.97	5.6	870	470	1.78E+22	6.1±0.06	26.2	4.3	protostar	4	SMT
62	19411+2306	19:43:18.1	+23:13:59	0.07±0.03	31.1±0.9	0.02	13	9.63E+10	2.80E-06	7.40E+02	1.35	8.89	870	269	1.30E+22	32.65±0.06	...	2.5	protostar	5	SMT
63	S87	19:46:20.5	+24:35:34	0.18±0.04	21±0.6	0.05	9	2.40E+11	4.15E-06	1.30E+04	8.44	87.59	850	1113	5.91E+22	1.71	...	1.9	UCHII	1	SMT
64	K3-50A	20:01:45.6	+33:32:42	1.64±0.14	-24.3±0.2	0.25	18	2.19E+12	6.05E-04	5.10E+05	14.64	28.67	850	5830	1.03E+23	7.6	CHII	1	CSO
65	20050+2720	20:07:06.7	+27:28:53	0.11±0.02	5.4±1.1	0.02	12.4	1.70E+11	8.50E-07	6.10E+02	4.6	22.38	850	177	5.97E+22	18.82±0.19	19.3	1.1	protostar	4	SMT
66	20056+3350	20:07:31.5	+33:59:39	0.25±0.03	8.6±0.5	0.03	14.7	3.44E+11	4.62E-06	23.39±0.28	...	1.7	protostar	4	SMT	
67	G073.0633+01.7958	20:08:10.0	+35:59:24	0.26±0.04	-0.4±0.2	0.12	4.5	4.31E+11	3.26E-06	3.50E+03	2.46	4.55	850	67	3.68E+22	27.81±0.18	17.6	1.4	protostar	3	SMT
68	ON1	20:10:09.1	+31:31:37	2.28±0.06	11.5±0.2	0.27	25.5	3.04E+12	5.24E-04	2.60E+04	12.42±0.08	...	6	UCHII	1	SMT
69	20106+3545	20:12:31.3	+35:54:46	0.17±0.03	8±0.4	0.04	9.4	2.34E+11	2.78E-06	13.94±0.18	...	1.6	protostar	4	SMT

Table 1 continued

No	Name	R.A J2000	Dec J2000	$\int T_{\text{mb}} d\nu$ K km s ⁻¹	v_{lsr} km s ⁻¹	T_{mb} K	FWZP km s ⁻¹	$N(\text{SiO})$ cm ⁻²	L_{SiO} L _⊙	L_{bol} L _⊙	F_{ν} Jy beam ⁻¹	S_{ν} Jy	λ μm	M_{gas} M _⊙	$N(\text{H}_2)$ cm ⁻²	$S_{22\mu\text{m}}$ Jy	T_{k} K	D kpc	Type	Ref	Telescope
70	20126+4104	20:14:26.0	+41:13:32	2.05±0.15	-3.7±0.8	0.11	46	2.89E+12	2.31E-04	4.00E+03	6.38	13.48	850	1194	6.37E+22	83.68±0.15	23.1	4.2	protostar	4	SMT
71	20188+3928	20:20:39.3	+39:37:52	0.71±0.05	0.7±0.3	0.07	27.5	9.77E+11	1.81E-05	2.20E+03	187.34±1.38	...	2	protostar	4	SMT
72	ON2S	20:21:41.0	+37:25:29	1.93±0.17	-2.3±0.8	0.11	39	2.71E+12	3.73E-04	2.90E+02	10.86	18.95	850	1212	4.57E+22	...	45.1	5.5	HII	1	SMT
73	ON2N	20:21:43.9	+37:26:39	2.22±0.12	-0.2±0.3	0.22	22	2.96E+12	4.29E-04	1.50E+04	13.17	31.14	850	3316	9.23E+22	148.4±0.14	...	5.5	CHII	1	SMT
74	S106	20:27:25.7	+37:22:52	0.27±0.03	-5.9±0.6	0.04	16	3.60E+11	2.90E-05	...	6.89	21.57	850	1277	4.83E+22	4.1	UCHII	1	SMT
75	20286+4105	20:30:27.9	+41:15:48	0.29±0.05	-2.4±0.7	0.04	17.2	3.99E+11	2.54E-05	1.10E+03	3.7	protostar	4	SMT
76	20293+3952	20:31:10.7	+40:03:10	1.14±0.09	12±0.9	0.08	42	1.72E+12	3.21E-05	3.50E+02	4.58	15.24	850	412	5.59E+22	174.52±0.64	20.1	2.1	protostar	5	SMT
77	G083.7962+03.3058	20:33:48.0	+45:40:54	1.08±0.05	-9.3±0.6	0.11	19.5	1.44E+12	1.35E-05	1.20E+04	1.4	HII	3	SMT
78	20333+4102	20:35:09.5	+41:13:18	0.27±0.04	4.6±0.5	0.04	11.5	3.71E+11	4.42E-06	25.04±0.28	...	1.6	protostar	4	SMT
79	G080.8645+00.4197	20:36:52.0	+41:36:24	0.29±0.04	-3.5±0.6	0.06	10.5	3.87E+11	3.63E-06	4.80E+03	174.84±0.64	...	1.4	HII	3	SMT
80	G080.8624+00.3827	20:37:00.0	+41:34:55	0.16±0.03	-0.3±0.3	0.04	6.5	2.13E+11	2.00E-06	2.00E+03	5.17	15.58	850	98	3.32E+22	2.47±0.05	32.1	1.4	protostar	3	SMT
81	G081.8652+00.7800	20:38:35.0	+42:37:13	2.77±0.1	10.9±0.2	0.33	19.5	3.70E+12	3.47E-05	4.90E+03	33.58	81.35	850	467	1.96E+23	79.99±0.44	34.6	1.4	protostar	3	SMT
82	G081.8789+00.7822	20:38:37.0	+42:37:58	0.7±0.1	10.5±0.6	0.12	15	9.34E+11	8.77E-06	1.10E+04	917.57±4.23	...	1.4	HII	3	SMT
83	G081.7131+00.5792	20:38:57.0	+42:22:40	0.48±0.07	1.8±0.9	0.05	18.5	6.60E+11	6.01E-06	3.60E+03	109.31±0.6	...	1.4	protostar	3	SMT
84	DR21S	20:39:00.8	+42:19:29	11.12±0.23	-0.9±0.2	0.65	43	1.48E+13	6.39E-04	6.90E+02	31.42	110.09	850	3488	2.20E+23	731.54	...	3	UCHII	1	CSO
85	G081.7220+00.5699	20:39:01.0	+42:22:50	7.79±0.15	-2.9±0.1	0.86	25.5	1.04E+13	9.75E-05	1.90E+03	34.15	64.35	850	408	2.20E+23	10.47±0.25	32	1.4	HII	3	SMT
86	G081.7522+00.5906	20:39:01.0	+42:24:59	0.95±0.08	-2.3±0.7	0.08	31.5	1.40E+12	1.19E-05	9.00E+03	9.24	36.55	850	415	1.07E+23	40.72±1.31	20.9	1.4	protostar	3	SMT
87	G081.7133+00.5589	20:39:02.0	+42:21:58	1.07±0.08	-3.2±0.2	0.2	12	1.43E+12	1.34E-05	9.10E+03	16.7	51.38	850	378	1.25E+23	44.45±0.66	28.6	1.4	HII	3	SMT
88	G081.7624+00.5916	20:39:03.0	+42:25:29	2.98±0.16	3.5±0.8	0.17	37.5	4.68E+12	3.73E-05	2.00E+03	7.69	25.27	850	333	1.03E+23	...	18.9	1.4	protostar	3	SMT
89	G97.53+3.19	21:32:11.4	+55:53:55	0.44±0.04	-71.4±0.5	0.04	25.5	5.87E+11	1.34E-04	1.00E+04	7.01±0.09	...	6.9	HII	1	SMT
90	G094.4637-00.8043	21:35:09.0	+50:53:09	1.35±0.1	-47.2±0.5	0.17	19	1.86E+12	2.16E-04	2.10E+04	39.76±0.04	...	5	protostar	3	SMT
91	21391+5802	21:40:42.4	+58:16:10	3.18±0.19	3.4±0.7	0.14	57	4.37E+12	1.30E-05	1.93±0.04	...	0.8	protostar	4	SMT
92	BFS11-B	21:43:06.7	+66:07:04	0.23±0.03	-8.5±0.5	0.05	14.5	3.07E+11	9.18E-06	41.48±0.08	...	2.5	HII	1	SMT
93	G105.5072+00.2294	22:32:23.0	+58:18:58	0.14±0.02	-52.1±0.3	0.05	36	1.93E+11	1.89E-05	7.00E+03	15.23±0.08	...	4.6	protostar	3	SMT
94	22506+5944	22:52:38.6	+60:00:56	1.22±0.09	-48.3±0.4	0.11	27	1.64E+12	2.53E-04	4.20E+04	5.71	13.32	850	1638	4.30E+22	27.46±0.2	28.4	5.7	protostar	4	SMT
95	23033+5951	23:05:25.5	+60:08:06	0.41±0.06	-51.2±0.7	0.05	22.5	5.64E+11	3.21E-05	9.67±0.09	...	3.5	protostar	5	SMT
96	NGC7538	23:13:44.8	+61:26:50	5.11±0.1	-55.2±0.1	0.54	37.5	6.85E+12	2.56E-04	4.60E+03	14.64	47.72	850	1416	1.10E+23	46.71±0.13	28.4	2.8	UCHII	1	SMT
97	NGC7538A	23:13:45.6	+61:28:18	2.62±0.07	-57.2±0.1	0.36	18.5	3.49E+12	2.05E-04	...	19.59	60.16	850	2507	1.33E+23	...	30.8	3.5	UCHII	2	CSO
98	G111.5671+00.7517	23:14:01.0	+61:27:19	0.63±0.06	-58.8±0.9	0.06	27	8.55E+11	2.93E-05	2.30E+04	4.7	18.03	850	546	3.88E+22	138.62±0.64	26.5	2.7	protostar	3	SMT
99	S157	23:16:04.4	+60:01:41	0.48±0.05	-42.7±0.4	0.06	17	6.40E+11	1.92E-05	1.30E+04	3.63	15.08	850	329	2.52E+22	51.65±0.86	30.2	2.5	CHII	1	SMT
100	23139+5939	23:16:08.7	+59:55:18	0.81±0.07	-45.5±0.4	0.09	17	1.09E+12	1.19E-04	1.10E+04	4.28	6.21	850	560	3.33E+22	...	27.7	4.8	protostar	5	SMT
101	23151+5912	23:17:21.0	+59:28:49	0.44±0.04	-54.5±0.3	0.07	22.3	6.05E+11	9.13E-05	1.10E+03	2.35	4.37	850	638	2.10E+22	138.5±0.26	...	5.7	protostar	5	SMT
102	23385+6053	23:40:53.2	+61:10:21	0.36±0.04	-49.3±0.7	0.06	12.5	4.95E+11	1.10E-04	2.08±0.06	...	6.9	protostar	4	SMT

Table 1 continued

Table 3. The parameters of sources without SiO 5-4 detection.

No	Name	R.A. (J2000) hh:mm:ss	Dec. (J2000) dd:mm:ss	v_{lsr} kms ⁻¹	Distance kpc	Type	Ref	Telescope
1	00117+6412	00:14:27.7	+64:28:46	-36.3	1.8	protostar	4	SMT
2	00420+5530	00:44:57.6	+55:47:18	-51.2	7.7	protostar	4	SMT
3	G125.6045+02.1038	01:16:36.0	+64:50:38	-53.7	4.1	UCHII	3	SMT
4	G125.7795+01.7285	01:17:53.0	+64:27:14	-64.5	5.2	protostar	3	SMT
5	G132.1570-00.7241	02:08:05.0	+60:46:02	-55.6	4.5	HII	3	SMT
6	G134.2792+00.8561	02:29:01.0	+61:33:30	-51.5	2	protostar	3	SMT
7	G136.3833+02.2666	02:50:08.0	+61:59:52	-42.4	3.3	protostar	3	SMT
8	G138.2957+01.5552	03:01:31.0	+60:29:13	-38	2.9	protostar	3	SMT
9	G139.9091+00.1969	03:07:24.0	+58:30:43	-39.5	3.2	UCHII	3	SMT
10	G142.2446+01.4299	03:27:31.0	+58:19:21	-46.7	4.2	HII	3	SMT
11	G141.9996+01.8202	03:27:38.0	+58:47:00	-13.9	0.8	protostar	3	SMT
12	04579+4703	05:01:39.7	+47:07:23	-16.5	2.5	protostar	4	SMT
13	05168+3634	05:20:16.2	+36:37:21	-15.1	6.1	protostar	4	SMT
14	05345+3157	05:37:47.8	+31:59:24	-18.4	1.8	protostar	4	SMT
15	05490+2658	05:52:12.9	+26:59:33	0.8	2.1	protostar	5	SMT
16	G192.5843-00.0417	06:12:53.0	+18:00:26	8.8	2	HII	3	SMT
17	G192.6005-00.0479	06:12:54.0	+17:59:23	7.4	2	protostar	3	SMT
18	G194.9349-01.2224	06:13:16.0	+15:22:43	15.9	2	protostar	3	SMT
19	G207.2654-01.8080	06:34:37.0	+04:12:44	12.6	1	UCHII	3	SMT
20	G212.0641-00.7395	06:47:13.0	+00:26:06	45	4.7	protostar	3	SMT
21	RCW142	17:50:15.1	+28:54:32	17	2	UCHII	1	SMT
22	G9.62+0.10	18:06:14.8	+20:31:40	2.5	7	UCHII	1	SMT
23	G12.42+0.50	18:10:51.8	-17:55:56	17.7	2.1	UCHII	1	SMT
24	G12.89+0.49	18:11:51.6	-17:52:24	33.8	3.5	HII	1	SMT
25	G12.2-0.1	18:12:39.7	-18:24:20	24.4	3.7	CHII	1	SMT
26	G13.87+0.28	18:14:35.0	-16:15:37	49	4.4	HII	1	SMT
27	W33A	18:14:39.3	+17:52:11	36.6	4.5	HII	1	SMT
28	G015.31-00.16MM2	18:18:50.0	-15:43:19	31.1	3.2	IRDC	6	SMT
29	I18182-1433MM2	18:21:15.0	-14:33:06	41.1	3.6	IRDC	6	SMT
30	G023.60+00.00MM4	18:25:07.0	-08:18:21	53.8	3.9	IRDC	6	SMT
31	I18223-1243MM2	18:25:09.0	-12:44:15	45.3	3.7	IRDC	6	SMT
32	I18223-1243MM1	18:25:10.0	-12:42:26	45	3.7	IRDC	6	SMT
33	G022.35+00.41MM2	18:30:24.0	-09:12:44	60.2	4.3	IRDC	6	SMT
34	I18306-0835MM2	18:33:17.0	-08:33:26	76.7	2.5	IRDC	6	SMT
35	I18306-0835MM3	18:33:32.0	-08:32:29	53.9	2.5	IRDC	6	SMT
36	G023.60+00.00MM7	18:34:21.0	-08:17:11	54	3.9	IRDC	6	SMT
37	G23.95+0.16	18:34:23.8	+07:54:53	79.9	5.8	HII	1	SMT
38	G024.08+00.04MM2	18:34:51.0	-07:45:32	52.1	3.8	IRDC	6	SMT
39	G024.08+00.04MM1	18:34:57.0	-07:43:26	113.6	3.8	IRDC	6	SMT
40	G024.08+00.04MM3	18:35:02.0	-07:45:25	51.8	3.8	IRDC	6	SMT
41	G024.08+00.04MM4	18:35:03.0	-07:45:56	51.9	3.8	IRDC	6	SMT
42	G024.33+00.11MM11	18:35:05.0	-07:35:58	112.6	3.8	IRDC	6	SMT
43	G024.33+00.11MM6	18:35:08.0	-07:34:33	114.4	3.8	IRDC	6	SMT
44	G024.33+00.11MM4	18:35:19.0	-07:37:17	115.1	3.8	IRDC	6	SMT
45	G024.33+00.11MM9	18:35:26.0	-07:36:56	119.7	3.8	IRDC	6	SMT
46	I18337-0743MM2	18:36:28.0	-07:40:28	58.6	4	IRDC	6	SMT
47	G025.04-00.20MM2	18:38:18.0	-07:02:51	63.8	3.4	IRDC	6	SMT
48	G35.20-1.74	19:01:47.0	+01:13:08	43.6	3.5	UCHII	2	CSO

Reference. – (1) Shirley et al. (2003); (2) Li et al. (2015); (3) Maud et al. (2015b); (4) Zhang et al. (2005); (5) Sridharan et al. (2002); (6) Sakai et al. (2008).

No	Name	R.A. (J2000)	Dec. (J2000)	v_{lsr}	Distance	Type	Ref	Telescope
		hh:mm:ss	dd:mm:ss	kms ⁻¹	kpc			
49	19282+1814	19:30:28.1	+18:20:53	24.1	2.1	protostar	4	SMT
50	19374+2352	19:39:33.2	+23:59:55	36.9	4.3	protostar	4	SMT
51	19403+2258	19:42:27.2	+23:05:12	26.7	2.4	protostar	5	SMT
52	G59.78+0.06	19:43:11.6	+23:43:54	22.4	2.2	UCHII	1	SMT
53	19413+2332	19:43:28.9	+23:40:04	20.8	1.8	protostar	5	SMT
54	G61.48+0.09	19:46:47.3	+25:12:45	21.9	5.4	UCHII	2	CSO
55	19471+2641	19:49:09.9	+26:48:52	21	2.4	protostar	5	SMT
56	20051+3435	20:07:03.8	+34:44:35	11.6	1.6	protostar	5	SMT
57	20062+3550	20:08:09.8	+35:59:20	0.6	4.9	protostar	4	SMT
58	20081+2720	20:10:11.5	+27:29:06	5.7	0.7	protostar	5	SMT
59	20099+3640	20:11:46.4	+36:49:37	-36.4	8.7	protostar	4	SMT
60	20216+4107	20:23:23.8	+41:17:40	-20	1.7	protostar	5	SMT
61	20217+3947	20:23:31.7	+39:57:23	-0.9	3.7	protostar	4	SMT
62	20220+3728	20:23:55.7	+37:38:10	-2.7	4.5	protostar	4	SMT
63	G077.9550+00.0058	20:29:31.0	+39:01:20	-4.2	1.4	HII	3	SMT
64	20278+3521	20:29:46.9	+35:31:39	-4.5	5	protostar	4	SMT
65	G079.8749+01.1821	20:30:27.0	+41:15:59	-3.8	1.4	HII	3	SMT
66	G083.0936+03.2724	20:31:35.0	+45:05:45	-3	1.4	HII	3	SMT
67	G083.7071+03.2817	20:33:36.0	+45:35:44	-3.2	1.4	protostar	3	SMT
68	20319+3958	20:33:49.3	+40:08:45	8.8	1.6	protostar	5	SMT
69	20332+4124	20:34:59.9	+41:34:49	-20	3.9	protostar	5	SMT
70	20343+4129	20:36:07.1	+41:40:01	11.5	1.4	protostar	5	SMT
71	G080.9383-00.1268	20:39:25.0	+41:20:01	-1.2	1.4	HII	3	SMT
72	20444+4629	20:46:08.3	+46:40:41	-4.1	2.4	protostar	4	SMT
73	G085.4102+00.0032	20:54:14.0	+44:54:04	-36.5	5.5	protostar	3	SMT
74	21078+5211	21:09:25.2	+52:23:44	-6.1	1.5	protostar	4	SMT
75	G094.3228-00.1671	21:31:45.0	+51:15:35	-38.5	4.4	protostar	3	SMT
76	21307+5049	21:32:31.5	+51:02:22	-46.7	4.9	protostar	4	SMT
77	G094.6028-01.7966	21:39:58.0	+50:14:20	-43.9	4.9	protostar	3	SMT
78	21519+5613	21:53:39.2	+56:27:46	-63.2	7.3	protostar	4	SMT
79	22134+5834	22:15:09.1	+58:49:09	-18.3	2.6	protostar	5	SMT
80	22172+5549	22:19:09.0	+56:04:45	-43.8	2.9	protostar	4	SMT
81	22198+6336	22:21:27.6	+63:51:42	-11.1	1.3	protostar	4	SMT
82	22305+5803	22:32:24.3	+58:18:58	-52.1	5.4	protostar	4	SMT
83	G105.6270+00.3388	22:32:45.0	+58:28:18	-52.1	4.5	HII	3	SMT
84	G107.6823-02.2423	22:55:29.0	+58:09:24	-55.1	4.7	protostar	3	SMT
85	22551+6221	22:57:05.2	+62:37:44	-13.4	0.7	protostar	5	SMT
86	G108.7575-00.9863	22:58:47.0	+58:45:01	-50.8	4.3	protostar	3	SMT
87	G109.0775-00.3524	22:58:58.0	+59:27:36	-48.3	4	protostar	3	SMT
88	G109.0974-00.3458	22:59:05.0	+59:28:23	-46.7	3.8	HII	3	SMT
89	G108.4714-02.8176	23:02:32.0	+56:57:51	-53.9	4.5	protostar	3	SMT
90	23026+5948	23:04:45.7	+60:04:35	-51.1	5.8	protostar	4	SMT
91	G110.1082+00.0473	23:05:10.0	+60:14:47	-50.2	4.3	HII	3	SMT
92	G111.5234+00.8004	23:13:32.0	+61:29:06	-58	2.7	protostar	3	SMT
93	G111.5851+00.7976	23:14:01.0	+61:30:17	-56.5	2.7	protostar	3	SMT
94	23140+6121	23:16:11.7	+61:37:45	-51.5	6.4	protostar	4	SMT
95	G114.0835+02.8568	23:28:27.0	+64:17:38	-53.2	4.2	protostar	3	SMT
96	23314+6033	23:33:44.3	+60:50:30	-45.4	2.8	protostar	4	SMT
97	23545+6508	23:57:05.2	+65:25:11	-18.4	0.8	protostar	5	SMT

Table 2 continued

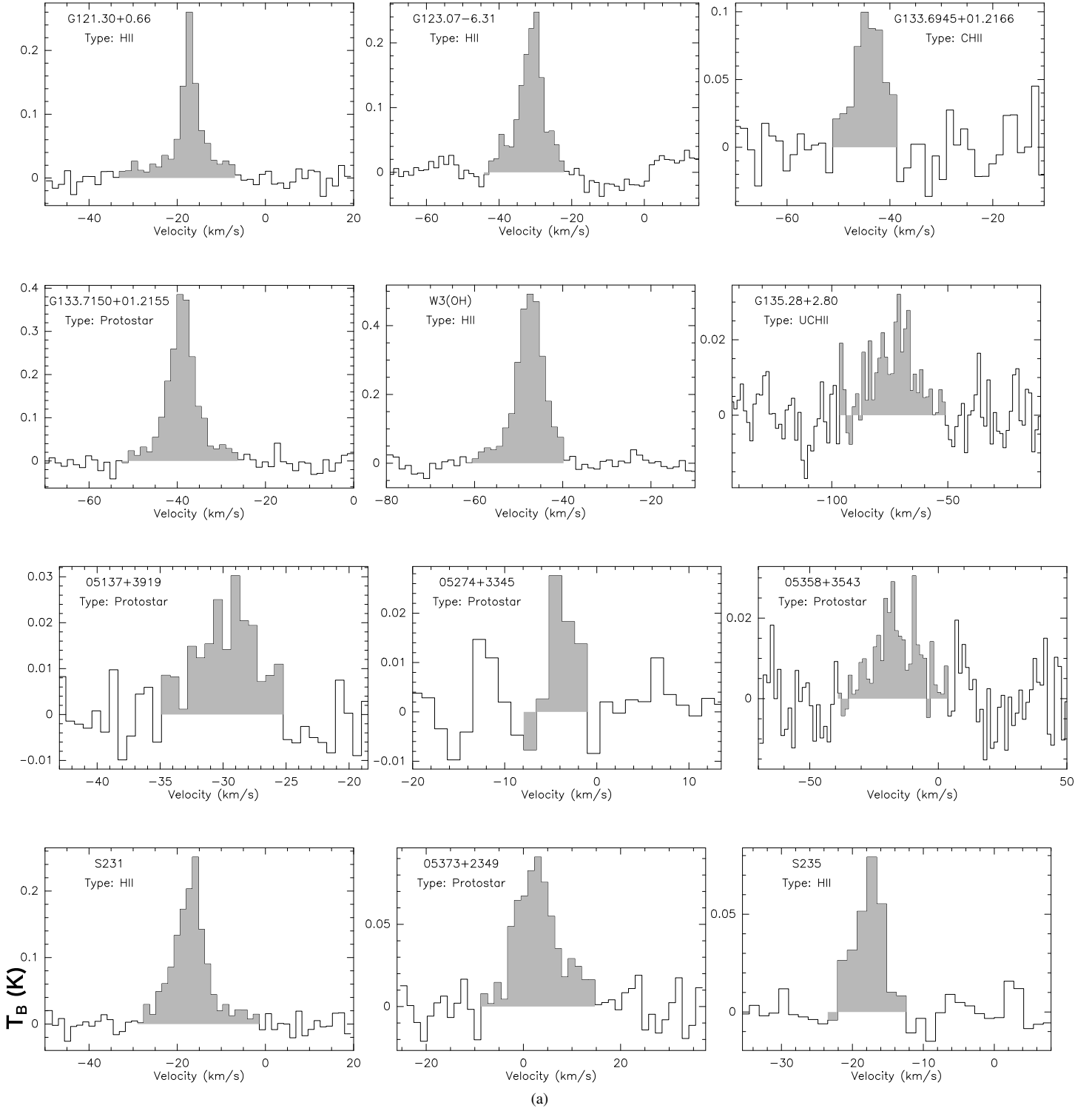
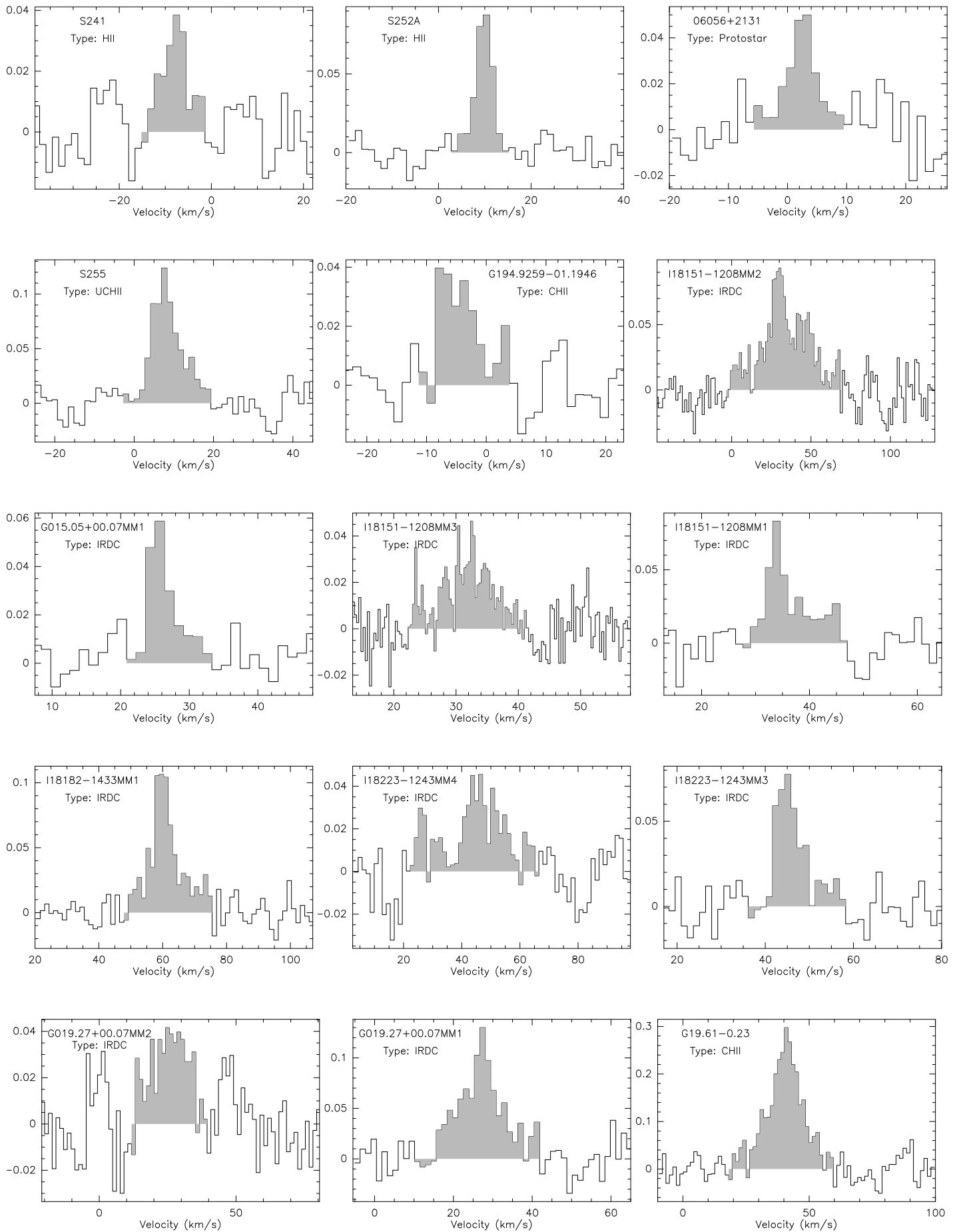


Figure A1. Spectral line of the SiO 5-4 transition in each source. The source name and type are presented in each panel.

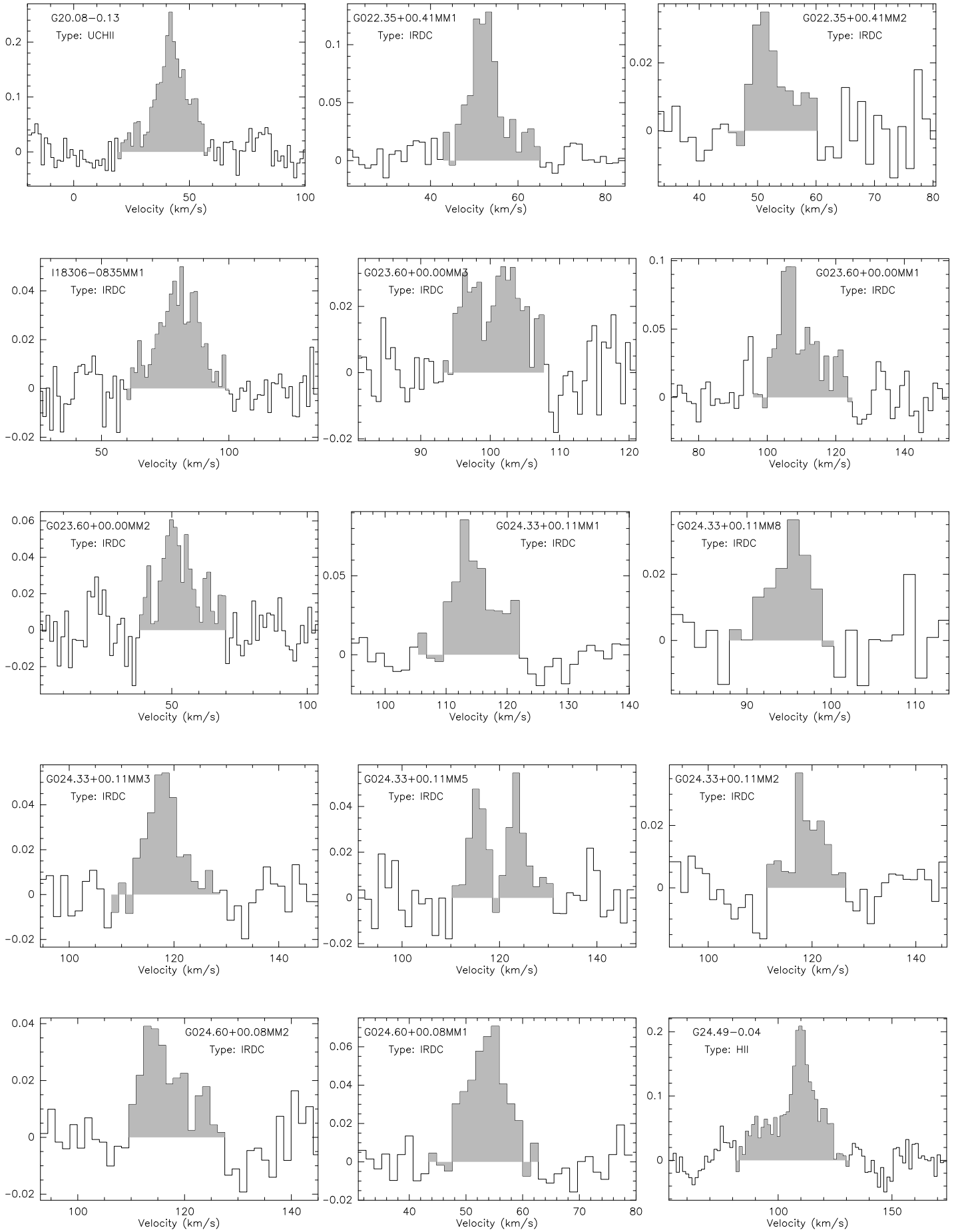
APPENDIX

A. APPENDIX INFORMATION



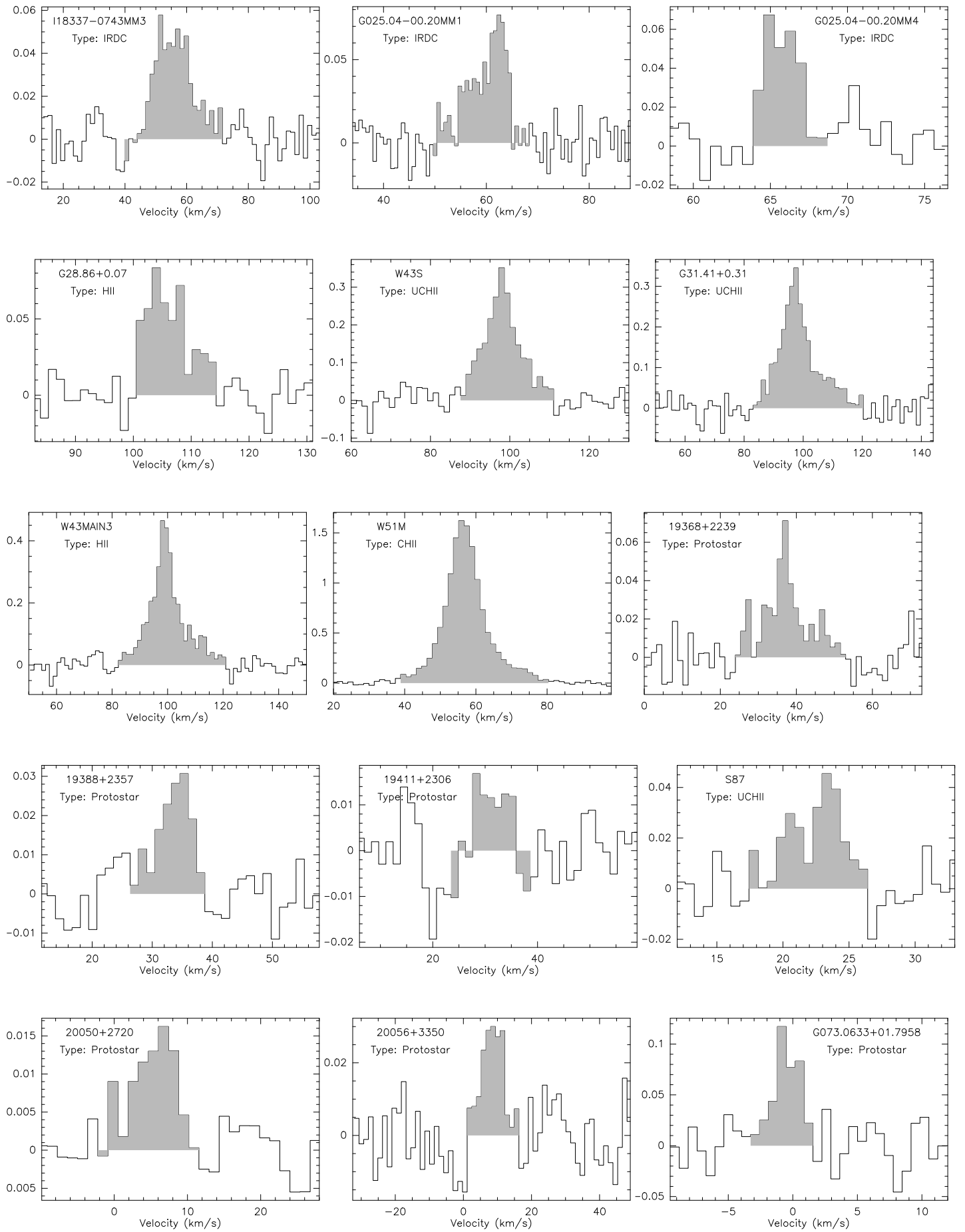
(b)

Figure A1. Continuation



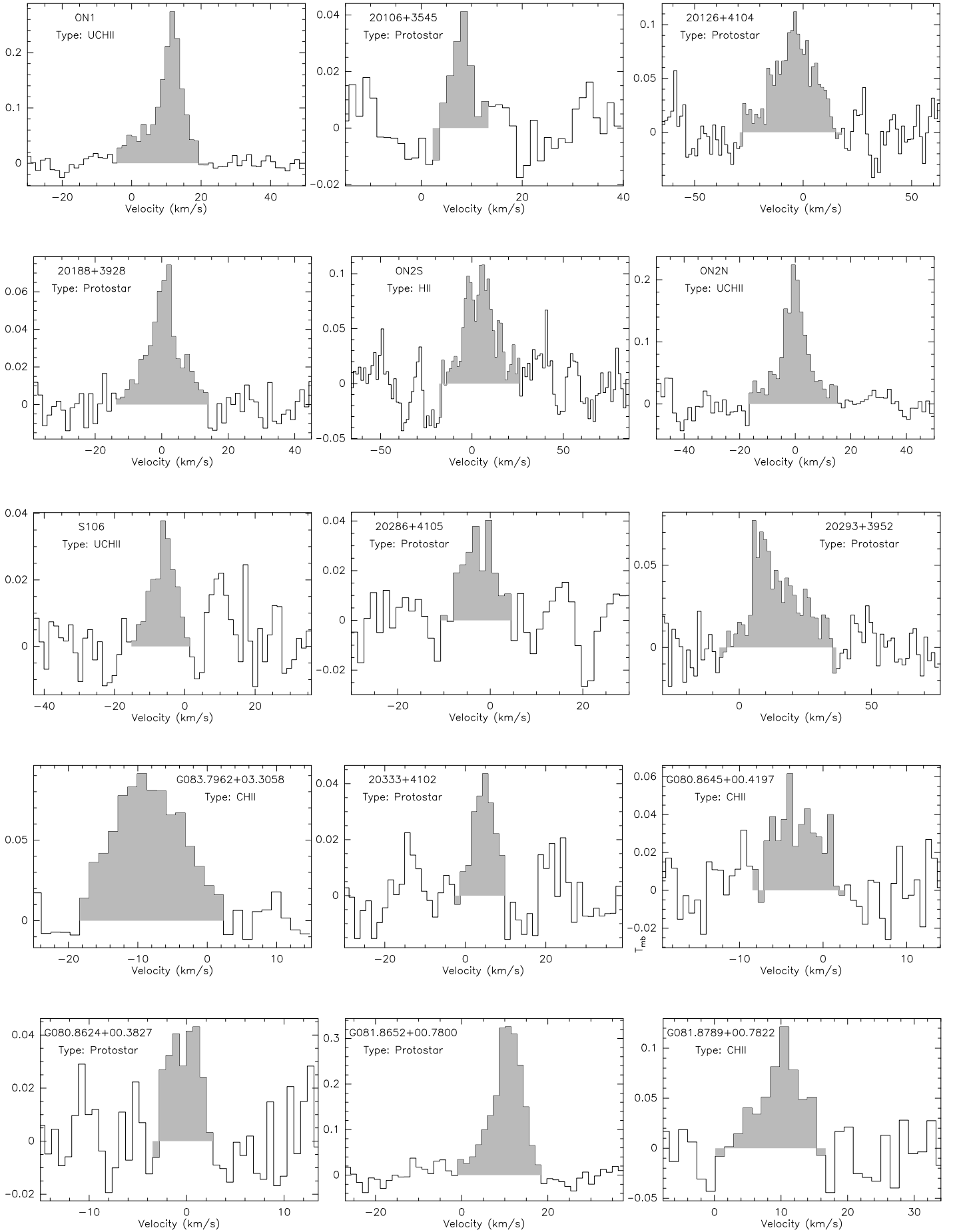
(c)

Figure A1. Continuation



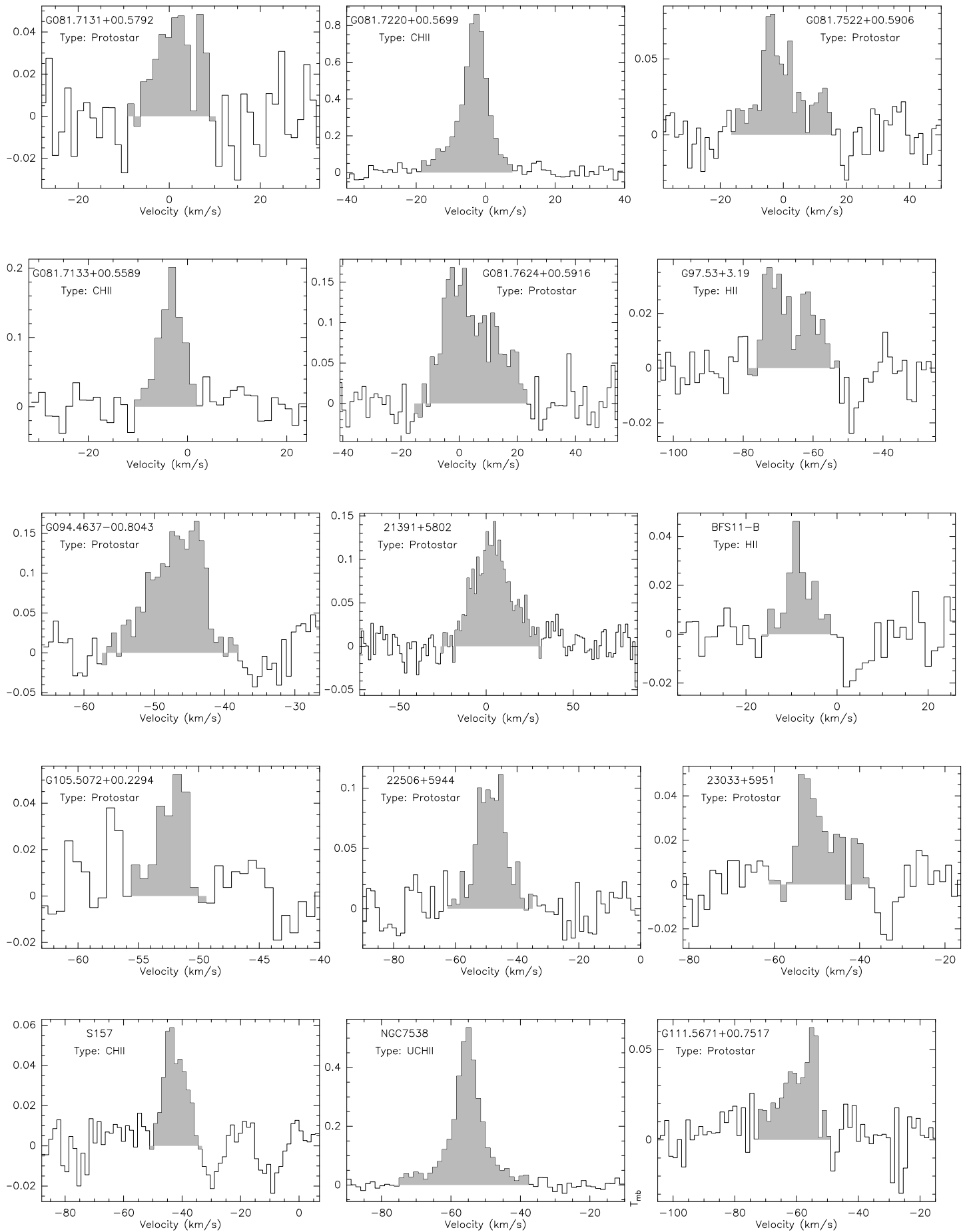
(d)

Figure A1. Continuation



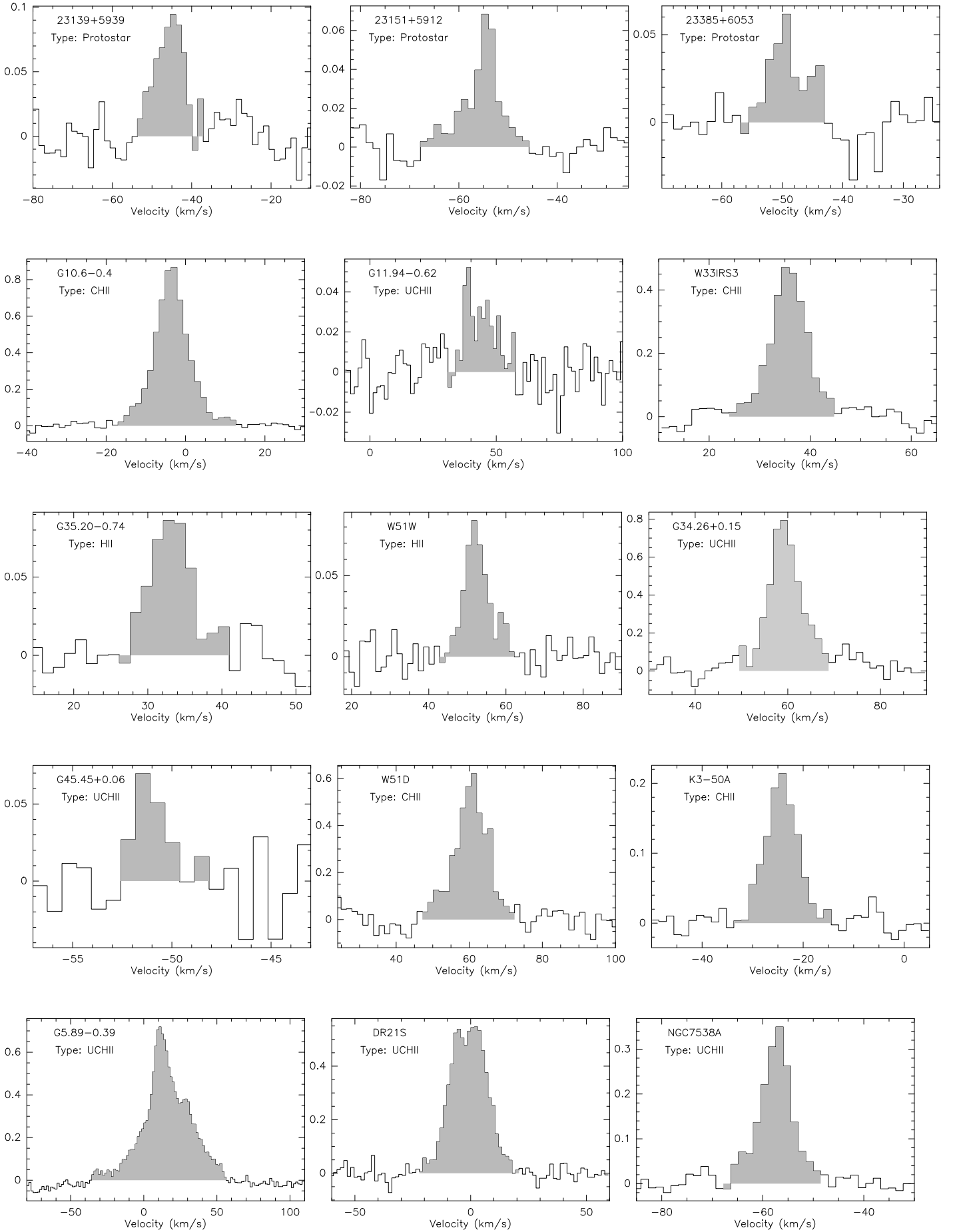
(e)

Figure A1. Continuation



(f)

Figure A1. Continuation



(g)

Figure A1. Continuation